NAVAL POSTGRADUATE SCHOOL

MONTEREY, CALIFORNIA

THESIS

DESIGN, IMPLEMENTATION, AND EVALUATION OF A SPARSE APERTURE TESTBED FOR IMAGE CORRECTION IN SMALL SATELLITE FORMATIONS

by

Raymond T. Yoo

December 2023

Thesis Advisor:	Jae Jun Kim
Co-Advisor:	Brij N. Agrawal

Approved for public release. Distribution is unlimited.

THIS PAGE INTENTIONALLY LEFT BLANK

REPORT DOCUMENTATION PAGE	*Form Approved OMB No. 0704-0188*

1. AGENCY USE ONLY ***(Leave blank)***	**2. REPORT DATE** December 2023	**3. REPORT TYPE AND DATES COVERED** Master's thesis

4. TITLE AND SUBTITLE DESIGN, IMPLEMENTATION, AND EVALUATION OF A SPARSE APERTURE TESTBED FOR IMAGE CORRECTION IN SMALL SATELLITE FORMATIONS	**5. FUNDING NUMBERS**
6. AUTHOR(S) Raymond T. Yoo	
7. PERFORMING ORGANIZATION NAME(S) AND ADDRESS(ES) Naval Postgraduate School Monterey, CA 93943-5000	**8. PERFORMING ORGANIZATION REPORT NUMBER**
9. SPONSORING / MONITORING AGENCY NAME(S) AND ADDRESS(ES) N/A	**10. SPONSORING / MONITORING AGENCY REPORT NUMBER**

11. SUPPLEMENTARY NOTES The views expressed in this thesis are those of the author and do not reflect the official policy or position of the Department of Defense or the U.S. Government.

12a. DISTRIBUTION / AVAILABILITY STATEMENT Approved for public release. Distribution is unlimited.	**12b. DISTRIBUTION CODE** A

13. ABSTRACT (maximum 200 words)

This thesis examines current sparse aperture technologies using multiple small satellites, with a focus on experimental simulation and testing using the Naval Postgraduate School (NPS) sparse aperture testbed. Sparse aperture studies researched by the National Aeronautics and Space Administration Jet Propulsion Laboratory study and previous NPS students served as the foundation for the sparse aperture testbed design and testing. The testbed incorporates three collector mirrors, each with six degrees of freedom for independent motion and tracking, complemented by a real-time laser metrology system for simulation of collector mirror satellites. A separate combiner platform with three piston-tip-tilt mirrors corrects optical aberrations caused by formation flying errors on the collector mirror satellites. The implementation of the sparse aperture concept into the experimental testbed provides means to study key sparse aperture technologies experimentally. The testbed's ability to induce disturbances on the collector mirrors and correct the resulting image through the laser metrology system and the combiner mirror platform establishes a research platform for future work in optical sparse aperture designs for real life space applications.

14. SUBJECT TERMS deep learning, spatial aperture	**15. NUMBER OF PAGES** 107
	16. PRICE CODE

17. SECURITY CLASSIFICATION OF REPORT Unclassified	**18. SECURITY CLASSIFICATION OF THIS PAGE** Unclassified	**19. SECURITY CLASSIFICATION OF ABSTRACT** Unclassified	**20. LIMITATION OF ABSTRACT** UU

NSN 7540-01-280-5500 Standard Form 298 (Rev. 2-89)
Prescribed by ANSI Std. 239-18

THIS PAGE INTENTIONALLY LEFT BLANK

DESIGN, IMPLEMENTATION, AND EVALUATION OF A SPARSE APERTURE TESTBED FOR IMAGE CORRECTION IN SMALL SATELLITE FORMATIONS

Raymond T. Yoo
Lieutenant, United States Navy
BA, University of Virginia, 2013

Submitted in partial fulfillment of the
requirements for the degree of

MASTER OF SCIENCE IN ASTRONAUTICAL ENGINEERING

from the

NAVAL POSTGRADUATE SCHOOL
December 2023

Approved by: Jae Jun Kim
Advisor

Brij N. Agrawal
Co-Advisor

Brian S. Bingham
Chair, Department of Mechanical and Aerospace Engineering

THIS PAGE INTENTIONALLY LEFT BLANK

ABSTRACT

This thesis examines current sparse aperture technologies using multiple small satellites, with a focus on experimental simulation and testing using the Naval Postgraduate School (NPS) sparse aperture testbed. Sparse aperture studies researched by the National Aeronautics and Space Administration Jet Propulsion Laboratory study and previous NPS students served as the foundation for the sparse aperture testbed design and testing. The testbed incorporates three collector mirrors, each with six degrees of freedom for independent motion and tracking, complemented by a real-time laser metrology system for simulation of collector mirror satellites. A separate combiner platform with three piston-tip-tilt mirrors corrects optical aberrations caused by formation flying errors on the collector mirror satellites. The implementation of the sparse aperture concept into the experimental testbed provides means to study key sparse aperture technologies experimentally. The testbed's ability to induce disturbances on the collector mirrors and correct the resulting image through the laser metrology system and the combiner mirror platform establishes a research platform for future work in optical sparse aperture designs for real life space applications.

THIS PAGE INTENTIONALLY LEFT BLANK

TABLE OF CONTENTS

I. INTRODUCTION 1
  A. BACKGROUND 1
  B. RESEARCH OBJECTIVES 3
  C. THESIS ORGANIZATION 4

II. TECHNICAL BACKGROUND 5
  A. SPARSE APERTURE IMAGING FUNDAMENTALS 5
  B. ADVANTAGES OF SPARSE APERTURE IMAGING 10
  C. SPARSE APERTURE ARCHITECTURE 15
  D. SPARSE APERTURE FORMATION FLYING 16
  E. CHALLENGES TO SPARSE APERTURE SYSTEMS 22
  F. PREVIOUS AND CURRENT RELATED SPARSE APERTURE PROJECTS 24

III. EXPERIMENTAL SETUP 29
  A. NPS SPARSE APERTURE TESTBED OVERVIEW 29
  B. TESTBED COMPONENTS 30
    1. Newport RS Table 30
    2. Light Point Source and Scene Image 31
    3. ThorLabs Nanomax 600 Series 6-DOF Simulator 32
    4. Optics Mirrors 33
    5. Laser Metrology System 36
    6. Combiner Spacecraft Platform 38
    7. Imaging Development System (IDS) Digital Camera 41
  C. TESTBED IMPLEMENTATION AND CHALLENGES 41

IV. METHODOLOGY FOR SIMULATION AND EXPERIMENT 43
  A. CALIBRATION 44
  B. SIMULATION MODEL AND SIMULATION SETUP 47
  C. OBSERVED METRICS 50

V. ANALYSIS 53
  A. RANDOM DISTURBANCES (RD) 53
    1. Applied Disturbances 53
    2. Interferometric Measurements 54

3. Applied Corrections 55
4. Images 57
5. PSF Comparison 59
B. NASA DISTURBANCES 62
1. Applied Disturbances 62
2. Interferometric Measurements 63
3. Applied Corrections 64
4. Images 66
5. PSF Comparison 68

VI. CONCLUSIONS AND FUTURE WORK 71
A. CONCLUSIONS 71
B. FUTURE WORK 72
1. Wavefront Sensing and Metrology System 72
2. Resolution Analysis Using Diverse Test Images 73
3. Sparse Aperture Testbed Improvements 74
4. Computer Modeling 74

APPENDIX: MATLAB SCRIPT FOR TESTBED 77

LIST OF REFERENCES 83

INITIAL DISTRIBUTION LIST 87

LIST OF FIGURES

Figure 1. Price vs. primary diameter of telescopes. Source: [1]. 2

Figure 2. Golay-4 array configuration. Source: [5]. 7

Figure 3. Ground based Golay arrays vs. monolith hardware costs. Source: [1]. 12

Figure 4. Ground based Golay arrays vs. monolith hardware and labor costs. Source: [1]. 12

Figure 5. Small satellite classifications. Source: [7]. 13

Figure 6. CubeSat configuration. Source: [6]. 14

Figure 7. NASA JPL sparse aperture formation architectures. Source: [4]. 16

Figure 8. Orbit satellite formation. Source: [4]. 17

Figure 9. Leader/Follower (L/F) architecture. Source: [10]. 17

Figure 10. Center of Formation (COF) architecture. Source: [10]. 18

Figure 11. Hybrid L/F and COF architecture. Source: [10]. 19

Figure 12. Formation orbital reference point. Source: [10]. 20

Figure 13. MEO disturbances. Source: [10]. 20

Figure 14. L/F formation control performance. Source: [10]. 21

Figure 15. PSF plot of Golay-3 array. Source: [11]. 22

Figure 16. OPTIIX laser metrology system. Source: [10]. 23

Figure 17. Golay3 system. Source: [13]. 24

Figure 18. Final ARGOS system configuration. Source: [1]. 25

Figure 19. Two collector mirror testbed design. Source: [4]. 27

Figure 20. Three-mirror design testbed. Source: [14]. 30

Figure 21. Newport RS seismically isolated table. Source: [15]. 31

Figure 22. USAF resolution test target. 32

Figure 23. Thorlabs 6-DOF motion simulators. Source: [17]. 33

Figure 24. Sparse aperture array design. Source: [14]. 34

Figure 25. Corner cubes on collector mirror. 35

Figure 26. Sparse aperture testbed parabolic mirror. 36

Figure 27. Laser metrology system for NPS testbed. Source: [14]. 37

Figure 28. Combiner sparse array layout. 39

Figure 29. Combiner mirror stage. Source: [17]. 40

Figure 30. Combiner platform. 40

Figure 31. Ideal aligned 3-mirror collectors from computer simulation: flower pattern. 45

Figure 32. Sparse aperture trajectory simulation. 48

Figure 33. L/F formation flyover of Ukraine. 49

Figure 34. RD: Applied disturbances to collector mirrors. 54

Figure 35. RD: Laser interferometer measurements. 55

Figure 36. RD: Tip/tilt corrections to combiner mirrors. 56

Figure 37. RD: Piston corrections to combiner mirrors. 57

Figure 38. RD: Panchromatic and USAF test images. 58

Figure 39. RD: Initial PSF for panchromatic light. 59

Figure 40. RD: Corrected PSF for panchromatic light. 60

Figure 41. RD: Uncorrected PSF for panchromatic light. 60

Figure 42. NASA: Applied disturbances to combiner mirrors. 63

Figure 43. NASA: Laser interferometer measurements. 64

Figure 44. NASA: Tip/tilt corrections to combiner mirrors. 65

Figure 45. NASA: Piston corrections to combiner mirrors. 65

Figure 46. NASA: Panchromatic and USAF test images. 67

Figure 47. NASA: Initial PSF for panchromatic light.. 68

Figure 48. NASA: Corrected PSF for panchromatic light. 69

Figure 49. NASA: Uncorrected PSF for panchromatic light. 69

THIS PAGE INTENTIONALLY LEFT BLANK

LIST OF TABLES

Table 1. Sparse aperture simulation orbital elements. 50

Table 2. Random disturbance panchromatic light metrics.................................... 62

Table 3. NASA disturbances panchromatic light metrics..................................... 70

THIS PAGE INTENTIONALLY LEFT BLANK

LIST OF ACRONYMS AND ABBREVIATIONS

ADC	analog to digital converter
ARGOS	Adaptive Reconnaissance Golay-3 Optical Satellite
BL	bottom left
BLC	bottom left center
BRC	bottom right center
CCD	charge coupled device
COF	center of formation
dB	decibel
DOD-SP	Department of Defense- Space Policy
D	diameter
DOF	degrees of freedom
FWHM	full width at half maximum
GEO	geosynchronous orbit
Golay-N	Golay-Number
GSD	ground sample distance
IDS	image development system
ISS	International Space System
LDG	laser distance gauge
LEO	low Earth orbit
L/F	leader/follower
MEO	medium Earth orbit
MET	laser metrology-based control
MIT	Massachusetts Institute of Technology
MTF	modulation transfer function

NASA JPL	National Aeronautics and Space Administration Jet Propulsion Laboratory
NPS	Naval Postgraduate School
OPD	optical path difference
OTF	optical transfer function
PI	Physik Instrumente
PISLR	peak-to-integral-sidelobe-ratio
PSF	point spread function
PSNR	peak signal to noise ratio
RD	random disturbances
RMSE	root mean square error
SRDC	Spacecraft Research and Design Center
TLC	top left center
TR	top right
USAF	United States Air Force
VME	virtual machine environment
WFS&C	wavefront sensor and control

ACKNOWLEDGMENTS

I give my deepest gratitude to Dr. Brij Agrawal and Dr. Jae Jun Kim for their mentorship, knowledge, and encouragement throughout this thesis journey. I thank Dr. Kim for his patience with my many questions. I would like to thank the SRDC and specifically Dr. Ty Martinez for help in setting up and teaching me how to use the sparse aperture test table.

I thank the United States Navy and Information Professional (IP) community for giving me the opportunity to study at the Naval Postgraduate School (NPS).

Finally, I want to thank my wife Koo and our beautiful children for all their love and support in everything I do.

THIS PAGE INTENTIONALLY LEFT BLANK

I. INTRODUCTION

This chapter introduces the background of sparse aperture imaging, outlines the research objectives guiding this thesis, and details the organizational structure of the paper.

A. BACKGROUND

Angular resolution, defined by the Rayleigh criterion, stands as a critical metric in astronomical observations [1]. It quantifies the capability of an optical system to differentiate between two proximate point sources [1]. As the boundaries of observational astronomy expand, the need for superior angular resolution increases. This resolution is directly linked to the aperture size of the observing instrument which is given by the equation [1]

$$\theta = 1.22 * \frac{\lambda}{D}, \tag{1}$$

where θ represents the angular resolution, λ denotes the wavelength of light, and D signifies the diameter of the aperture [1]. Given this relationship, there is a natural inclination towards telescopes with larger apertures. However, the size of the main mirror in space telescopes is limited by the payload size and weight that current space launch vehicles can handle, in addition to the cost-scaling rules of production [2]. Meinel's scaling laws predict a significant increase in manufacturing costs for apertures, with expenses rising in proportion to $D^{2.58}$ [1]. The graph in Figure 1 shows that even the production expenses of telescopes rise in direct proportion to $D^{2.76}$.

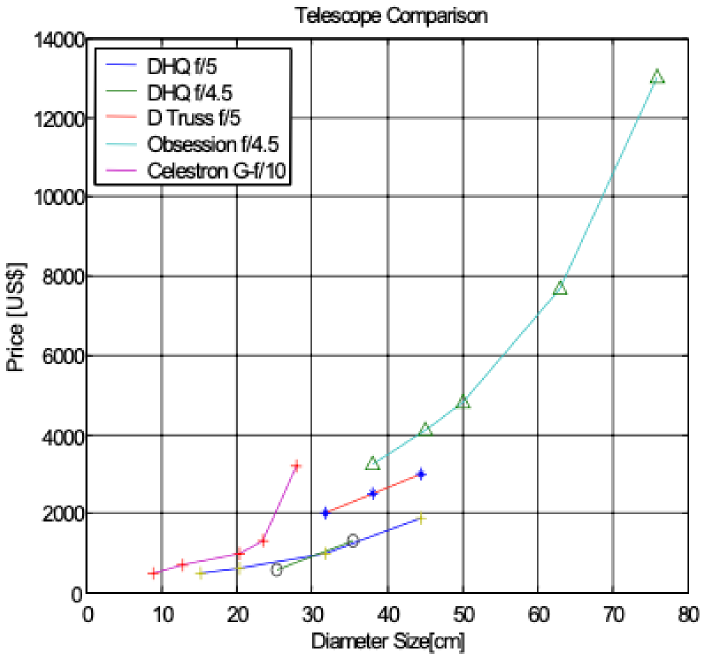

Figure 1. Price vs. primary diameter of telescopes. Source: [1].

On December 25, 2021, the James Webb Space Telescope, the most advanced and largest space telescope to date, was launched from Kourou, French Guiana [3]. It has a 6.5 m diameter and a light-collecting area of approximately 25 m^2. This project cost over 10 billion dollars and weighs around 6,500 kg [3]. While its capabilities are unmatched, the telescope's immense size posed significant challenges. To fit within the constraints of its launch vehicle, the Arianne V, the telescope's design incorporated a folding mechanism, enabling the large primary mirror to fit within the rocket's fairing [3]. This telescope was seen as a revolutionary advancement in deep space observation. Yet, the intricacies and financial burdens of deploying such vast telescopes underscore the growing challenges in space exploration and observation. With increasing demands for higher resolution and extended observational durations, the constraints of design and economics become more pronounced.

The escalating demand for advanced image acquisition in the twenty-first century necessitates finding alternative, scalable solutions in the space observation domain. Innovative methods are essential to boost observational capabilities. The Optical Sparse

Aperture approach emerges as a promising solution. This specialized technique in remote sensing leverages multiple smaller satellites for earth observation, presenting a viable alternative to the obstacles associated with deploying larger satellites.

Positioning smaller collectors in strategic formations at elevated altitudes enables the system to capture consistent high-definition imagery. This setup mirrors the segmented mirror layout of the James Webb telescope, where each collector functions as a segment mirror, collaboratively forming a large diameter. Such an approach presents a potential solution to current surveillance challenges, circumventing the high costs, mass, and design challenges associated with large telescopes like the James Webb. With this potential in mind, the Department of Defense is demonstrating an on-orbit satellite system to assess the usefulness of sparse aperture systems for intelligence gathering.

However, before this system can be fully implemented, there are technical challenges to overcome. The Naval Postgraduate School (NPS) has created a laboratory testbed to examine the technical aspects of sparse aperture systems. This testbed focuses on understanding the dynamics of small satellite formation flying and how it impacts optical data collection.

As the need for space observation continues to grow, sparse aperture systems present a practical and cost-effective approach to meet the demands of future space-based imaging. Transitioning to a functional sparse aperture architecture presents technical challenges. To understand the challenges of designing and building a sparse aperture array, the Naval Postgraduate School's testbed was used to develop an advanced sparse aperture system that can simulate precise formation flying and the effects on image resolution. This thesis provides a detailed overview of the design and implementation methods of the NPS testbed, highlighting its importance in demonstrating the feasibility of precise formation tracking in controlled environments.

B. RESEARCH OBJECTIVES

This thesis is guided by three primary research objectives. The first objective is to measure the wavefront error by analyzing images taken from the sparse apertures. This will provide insight into the image quality produced by the sparse aperture system. The second objective involves subjecting the sparse aperture system to various disturbances to observe their impact on the image quality. This will help in understanding the system's vulnerabilities under different conditions. The third objective is to assess the sparse aperture system's ability to correct the errors and produce a compensated image.

C. THESIS ORGANIZATION

Chapter II provides a technical background on (1) the fundamentals of sparse aperture imaging; (2) the advantages of sparse aperture imaging; (3) sparse aperture architecture; (4) sparse aperture formation flying; (5) the challenges for sparse aperture imaging; (6) previous and current related sparse aperture projects. Chapter III provides information on the experimental setup on the Naval Postgraduate School Sparse Aperture Testbed. This chapter includes a background on the testbed components: (1) Newport RS Test Table; (2) Light Point Source and Scene Images; (3) Thorlabs Nanomax 600 Series 6-DOF Simulators; (4) Optics Mirrors; (5) Laser Metrology System; (6) Combiner Spacecraft Platform; (7) Imaging Development Systems (IDS) Digital Camera. Chapter IV provides the methodology for the Sparse Aperture Imaging Simulation and Experiment. This chapter also provides a background on the MATLAB model that was built to represent a Leader/Follower Satellite Sparse Aperture Formation. Furthermore, it describes the two testing disturbances that the satellite formation encountered: (1) Random Disturbances; (2) NASA Jet Propulsion Laboratory (JPL) study generated disturbances. Chapter V presents an analysis of the results, discussing the different metrics to assess the sparse apertures' ability to compensate for error. Finally, Chapter VI concludes the thesis, providing the study's findings, concluding remarks, and discussion for future research.

II. TECHNICAL BACKGROUND

This chapter provides the technical background on several key aspects: (1) the fundamentals of sparse aperture imaging; (2) the advantages of sparse aperture imaging; (3) sparse aperture architecture; (4) sparse architecture formation flying; (5) the challenges to sparse aperture; (6) previous and current related sparse aperture projects.

A. SPARSE APERTURE IMAGING FUNDAMENTALS

Imaging satellites equipped with large aperture space mirrors at higher altitudes can provide enhanced persistent surveillance capabilities. However, the deployment of cost-effective space mirrors with apertures in the range of 10 to 30 m poses significant challenges. These challenges arise primarily from launch constraints and the intricacies involved in achieving the required precision for optical surfaces. Typically, imaging satellites operate in a Low Earth Orbit (LEO), with an orbital distance between 200 to 1000 km [4]. This altitude allows for high-resolution imagery and a small Ground Sample Distance (GSD). However, the short orbital period of around 90 min in LEO results in limited imaging durations over specific areas [4]. In contrast, a Medium Earth Orbit (MEO), ranging from 10,000 to 20,000 km, offers extended overhead persistence [4]. Yet, while MEO provides decent resolution, maintaining a small GSD becomes challenging. Finally, a Geosynchronous Orbit (GEO) enables a satellite to remain overhead for up to 24 hours [4]. However, achieving high-resolution imagery from this altitude can be extremely costly, often making it impractical for many projects.

The resolution achieved in conventional imaging systems is directly linked to the diameter of the system's aperture or pupil. Consider for instance a satellite in MEO at an altitude of 20,000 km [4]. This positioning allows the satellite to persistently monitor a target for over five hours. Achieving a GSD of 1.0 m with a mean observational wavelength of 500 nm requires a primary mirror diameter of approximately 12.2 m for the satellite, as dictated by the Rayleigh criterion [4]. This criterion defines the diffraction-limited resolution which is given by the equation [4],

$$GSD = 1.22 * \frac{\lambda}{D} * R, \tag{2}$$

where λ represents the mean wavelength, d represents the primary mirror diameter, and R represents the range to target object [4].

Deploying a satellite with such a large aperture is infeasible due to current limitations of rocket technology. The aperture's diameter can be reduced if the GSD or altitude was lowered but this would sacrifice overhead persistence [4]. Sparse aperture systems offer a potential solution to this aperture size challenge. Instead of a single large aperture, sparse aperture imaging employs multiple smaller apertures, or subapertures, to gather light [4]. The collected light from these subapertures is then recombined to construct a single high-resolution image. This method, which draws upon principles like interferometry, allows optical systems to achieve enhanced resolution without the need of a single, large, continuous aperture [4].

This technique originated from the principles used in radio telescopes since the 1940s where they combine signals from multiple antennas to get a clearer picture of radio sources in space [5]. In radio interferometry, signals from each small antenna are collected, combined, and analyzed after detection, a process known as "post detection" [5]. To align these signals correctly, delay lines are used between the antennas and a correlator, a device to process signals from multiple antennas, to ensure a clear combined signal [5]. This is capable because radio waves are longer wavelengths. However, optical systems need to be incredibly precise in aligning their smaller lenses to combine light waves directly [5]. Current detectors can only measure the intensity of the light, which is essentially an average over time. It cannot detect both amplitude and the phase of a signal. As a result, interferometric beam combination requires phasing of the subaperture to within a fraction of a wavelength [5].

It is important to figure out how to place the sparse apertures in the most optimum arrangement before developing quantitative metrics to evaluate the accuracy and effectiveness of sparse aperture arrays. Golay-N sparse aperture imaging arrays are specific configurations designed to optimize the benefits of sparse aperture imaging [5]. These arrays consist of a number (N) of identical, circular subapertures that each capture and process light [5]. These subapertures are placed strategically so that the Golay-N arrays aim to maximize image resolution while efficiently utilizing space, shown in Figure 2 [5].

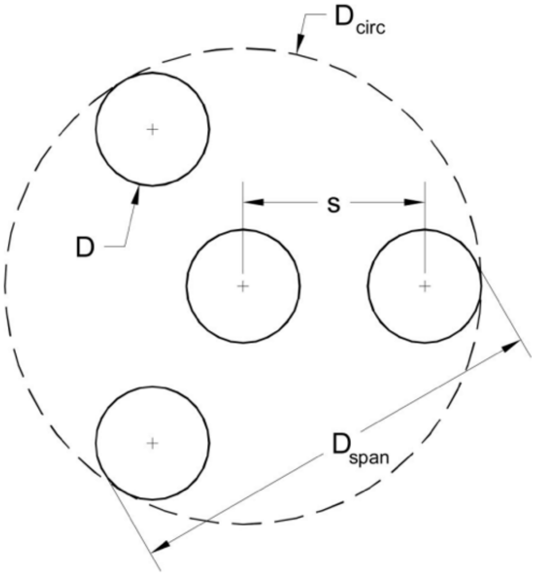

Figure 2. Golay-4 array configuration. Source: [5].

In Figure 2, ‘s’ represents the space between the centers of adjacent subapertures. ‘D’ represents the diameter of each individual subaperture [5]. The expansion factor, a ratio of ‘s’ to ‘D’, represents the spread of the subapertures, with a value of 1 when they touch [5]. D_{span} is the maximum distance between any two subapertures. D_{circ} is the diameter of the circle that surrounds all of the apertures [5]. The goal of this configuration is to have a small total subaperture area (A_{array}) while having a similar resolution to that of a single large aperture [5]. The concept of ‘fill factor’, denoted as ‘a’, quantifies the efficiency of area usage by comparing “the collective area of the sparse aperture setup to the area of a single, large aperture” that would provide a similar resolution. The aim is to achieve the lowest possible fill factor. The fill factor is given by the equation [5]

$$a = \frac{N}{D_{eff}^2}, \tag{3}$$

where D_{eff} represents the equivalent diameter of a single, large aperture that would produce an image of comparable quality to that of the sparse array configuration [5]. Having understood the foundational concepts of sparse aperture imaging, it is critical to understand the metrics that determine the quality of the images produced: Point Spread Function (PSF) and the Modulation Transfer Function (MTF) [5]. The PSF describes how a point source of light spreads out in an image and the MTF provides a measure of the imaging system's ability to reproduce varying levels of detail from the object being observed [5].

A deeper exploration into the mathematical derivation of the PSF is essential for a comprehensive understanding of its impact on imaging performance. The sparse array pupil function, denoted as $P_{array}(x,y)$, is the combined "view" or "function" of all the subapertures in the system [5]. Each individual subaperture is characterized by its own function $P_{sub}(x,y)$, its position coordinates (x_n, y_n), and a specific phase $\delta_n(x,y)$. The summation of all the individual subaperture functions is given by the equation [5]

$$P_{array}(x,y) = \sum_{n-1}^{N} P_{sub}(x-x_n, y-y_n)e^{\delta n(x,y)}. \tag{4}$$

The function $PSF_{array}(u,v)$ represents the incoherent PSF, incoherent meaning that light waves from different subapertures are not perfectly aligned or synchronized [5]. Equation (5) [5] describes how a point source of light would appear in an image taken by the sparse aperture system [5]. The performance of this system is determined by a variety of factors, such as the coordinates on the image plane (u, v), the horizontal and vertical components of the vector distances (Δx_k, Δy_k) separating the centers of adjacent subapertures, the light's wavelength (λ), and the focal length (f), which is the distance from the pupil plane to the image [5]. This is given by the equation [5]

$$PSF_{array}(u,v) = PSF_{sub}(u,v)\left[N + 2\sum_{k=1}^{\frac{N(N-1)}{2}} X\cos\left[\frac{2\pi}{\lambda f}\ (\Delta x_k u + \Delta y_k v)\right]\right]. \tag{5}$$

In an incoherent imaging system, the image created is a blend of the system's PSF and the perfect image [5]. Ideally, the system's PSF would be a single sharp point. For the best image quality, it is preferred to have a sharp central point in the PSF and minimal scattered light around it [5]. A sharper PSF implies that there would be a smaller FWHM, or full width at half maximum of the PSF, which implies a larger effective diameter. $D_{eff(PSF)}$, The effective diameter of the aperture based on the FWHM of its PSF is given by the equation [5]

$$D_{eff(PSF)} = \frac{\delta_0}{FWHM_{array\,PSF}} = \frac{1.03\lambda f}{FWHM_{array\,PSF}}. \tag{6}$$

Finally, the PISLR, or the Peak-to-Integrated-Sidelobe-Ratio compares the energy in the main peak of the PSF to the energy outside of it [5]. A high PISLR value indicates that most of the energy is concentrated in the main peak, while a lower value suggests a significant amount of energy in the sidelobes. High sidelobe energy indicates a reduction in the clarity of the final image [5]. Equation (7) [5] is the diameter of the main peak based on the effective diameter found in (6). The effective diameter essentially determines the region of interest around the main peak and sets the boundary for evaluating the energy within the primary peak, as opposed to the energy around it. This is given by the equation [5]

$$w_{peak} = \frac{2.44\lambda f}{D_{eff}}. \tag{7}$$

The PISLR calculation is the comparison of the energy inside and outside of the main peak and is given by the equation [5]

$$PISLR = 10log\,[\frac{\int_0^{2\pi}\iint_0^{w_{peak}} PSF_{array}(\rho,\phi)\rho d\rho d\phi}{\int_0^{2\pi}\iint_{w_{peak}}^{\infty} PSF_{array}(\rho,\phi)\rho d\rho d\phi}. \tag{8}$$

Ultimately, (4) describes how the entire sparse array is formed from individual subapertures. Equation (5) describes how the PSF of the entire array is formed from the PSFs of “N” subapertures. Equation (6) provides a way to measure the sharpness of the PSF. Equations (7) and (8) provide a way to measure how much energy is in the main peak of the PSF compared to the rest.

Evaluating the performance of an optical system, especially with extended objects like intelligence gathering on earth, requires more than a cursory glance at point sources.

The Modulation Transfer Function is another metric in the spatial frequency domain for evaluating imaging systems [5]. It describes how well an imaging system can transfer contrast from the object being observed to the image at varying levels of detail or spatial frequencies. The MTF is derived from the Optical Transfer Function (OTF), which is the normalized Fourier transform of the intensity PSF [5].

However, its application to sparse arrays brings forth challenges. Sparse arrays, characterized by their non-continuous apertures, exhibit a unique MTF profile with a significant drop in contrast in the mid spatial frequency range [1]. This implies potential difficulties in reproducing intermediate image details. Furthermore, the inherent geometry of sparse arrays, with their gaps in collecting area, results in an MTF that can be complex and less intuitive to interpret [1]. Side lobes present in the PSF of sparse arrays can further complicate the MTF, introducing oscillations that may not truly represent the system's imaging performance. Furthermore, ensuring coherence and alignment among the array's multiple subapertures is critical; any deviation can adversely affect the MTF [1].

The Modulation Transfer Function (MTF) offers insights into a system's capability to reproduce varying spatial frequencies. Ideally, a perfect system would maintain a constant MTF value across an infinite range [1].. However, practical systems face limitations, resulting in a finite MTF bandwidth and diminished image contrast [1]. While MTF plays a significant role in evaluating image quality, this study will concentrate primarily on the PSF metric.

B. ADVANTAGES OF SPARSE APERTURE IMAGING

Sparse aperture imaging offers several advantages, with cost-effectiveness standing out prominently. Compared to a monolithic array, sparse apertures are generally more affordable, aligning with the industry's shift towards maximizing efficiency while minimizing risks in space system development. Such an approach is vital given the substantial development costs and inherent risks associated with space missions, including potential mission failures.

A straightforward method for calculating the expense associated with deploying a sparse array system is based on a formula developed through research at the Massachusetts

Institute of Technology (MIT) [1]. This formula, detailed as (9) in the referenced study [1], offers a framework for estimating the financial outlay required for a sparse array payload. The key cost differentiators between a traditional monolithic system and a sparse aperture system are primarily found within the relay optics [1]. This includes the expenses related to the beam combiner, all elements of the relay optics pathway, and the essential actuators and electronics that facilitate active control over the beam combining process and is given by the equation [1]

$$Cost_{SparseArray} = Cost_{Telescope} + Cost_{RelayOptics} + Cost_{CCD}. \tag{9}$$

The cost-effectiveness of a Golay configuration is dependent on its effective diameter [1]. MIT's cost analysis study suggests that there exists a break-even point, after which sparse array systems, like the Golay configurations, become more cost-effective than monolithic systems of the same effective diameter [1]. For instance, in Figure 3, a Golay-3 configuration and a monolith array both have a cost of $400,000. However, the Golay-3 offers an effective aperture diameter that is over 50% larger than its monolithic counterpart. When labor costs are factored in, as shown in Figure 4, the advantages of the sparse Golay array further shift towards effective diameters. The overall system cost for these larger effective diameters is substantially lower for the Golay array than for a monolithic system. In summary, both Figures 3 and 4 illustrate a critical point: beyond the break-even point—where the cost lines for the two systems intersect—sparse aperture arrays not only become more cost-efficient but also deliver a superior effective aperture diameter compared to monolithic systems [1].

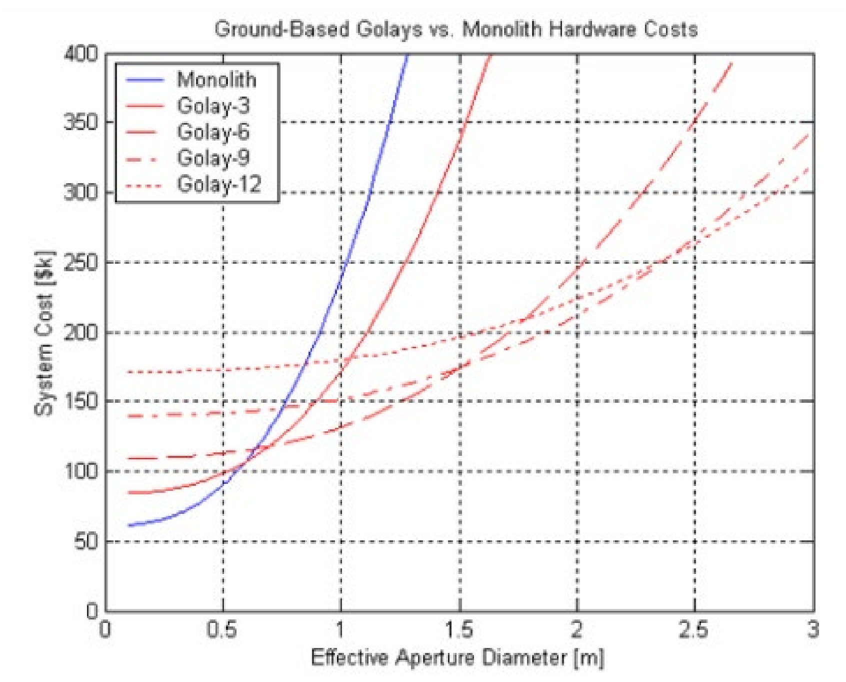

Figure 3. Ground based Golay arrays vs. monolith hardware costs. Source: [1].

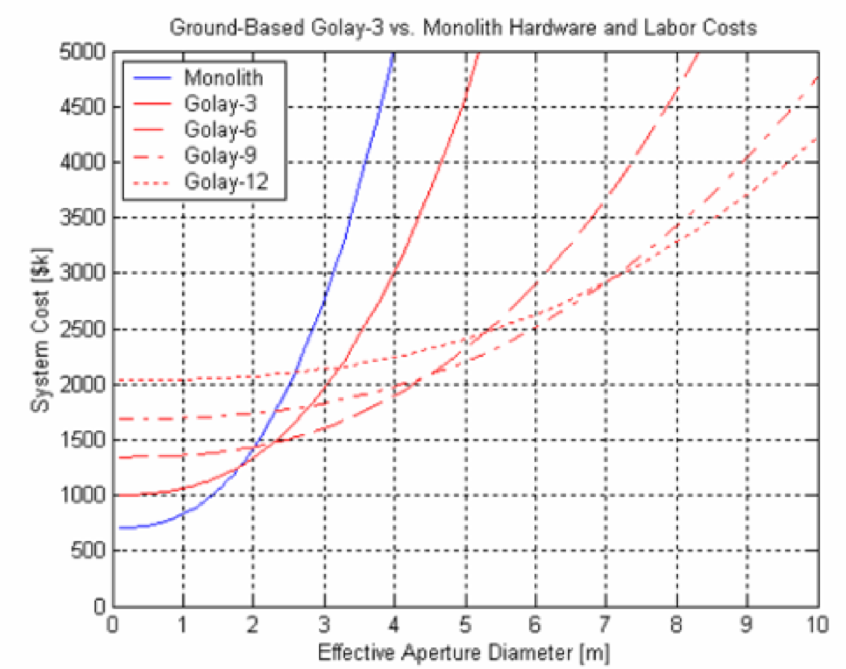

Figure 4. Ground based Golay arrays vs. monolith hardware and labor costs. Source: [1].

Another advantage of a sparse aperture system is the ability to use small satellites. With the growing importance of distributed systems and formation flying, small satellites have emerged as a primary platform for innovative missions. This thesis refers to the spacecraft in the experimental and simulation testing as small satellites. Small satellites are defined as a satellite of low mass and size. Though such satellites can be classified as "small," NASA suggests there are five classes of small satellites: "minisatellites weighing 100 to 180 kg;" "microsatellites weighing 10 to 100 kg;" "nanosatellites weighing 1 to 10 kg;" "picosatellites weighing .01 to 1 kg;" and "femtosatellites weighing 0.001 to 0.01 kg" [6]. Figure 5 displays the different types of small satellite classifications.

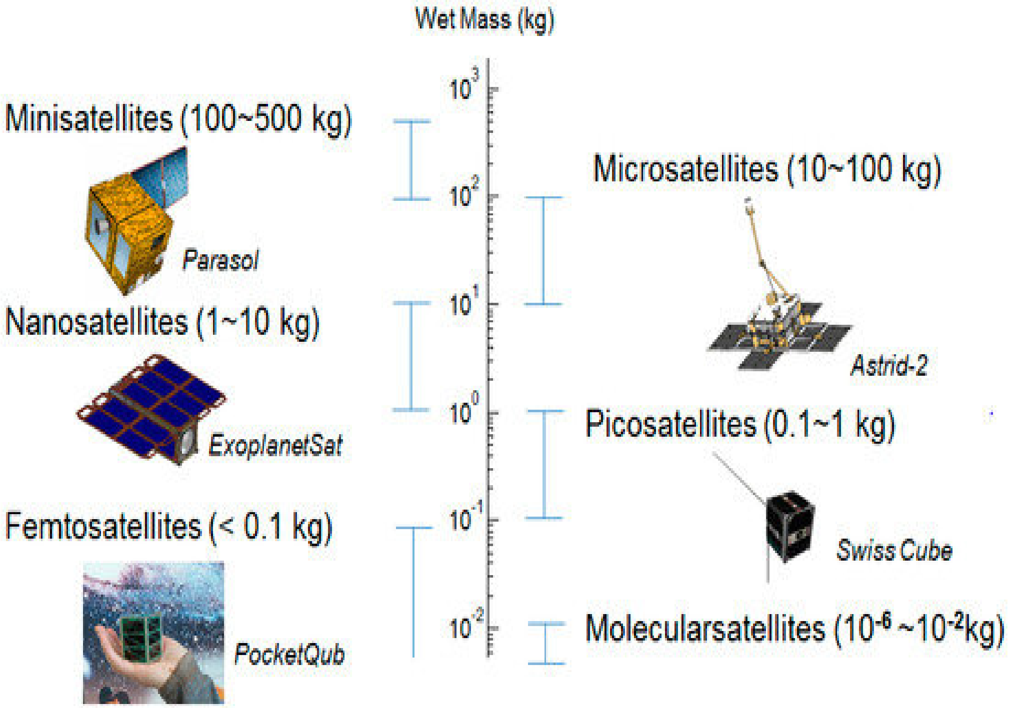

Figure 5. Small satellite classifications. Source: [7].

A primary reason for miniaturizing satellites is to reduce cost [8]. Larger satellites require the use of more powerful launch vehicles, which significantly increases the cost of satellite launches. By reducing the size and weight of satellites, it becomes feasible to use smaller, more economical launch vehicles. These vehicles are not only cheaper but can also deploy multiple small satellites simultaneously [8]. Additionally, the design and mass production of miniaturized satellites are more cost-effective compared to their larger counterparts. Beyond the cost benefits, small satellites offer unique functionalities. They can form constellations for low data rate communications, inspect larger satellites, facilitate university research, and test or qualify new hardware [8]. Pertinent to this thesis is the capability of CubeSats to operate in formation, enabling them to collectively gather data or imagery from specific Earth locations.

In recent times, CubeSats have gained significant attention in the field of satellite technology. These are a specific type of nanosatellites, characterized by a standardized size known as “one unit” or “1U,” which has dimensions of 10x10x10 cm [6]. CubeSats can vary in size, ranging from 1U up to 12U, as illustrated in Figure 6. However, it’s important to note that satellites involved in coordinated flight necessitate propulsion systems for maintaining their formation [6].

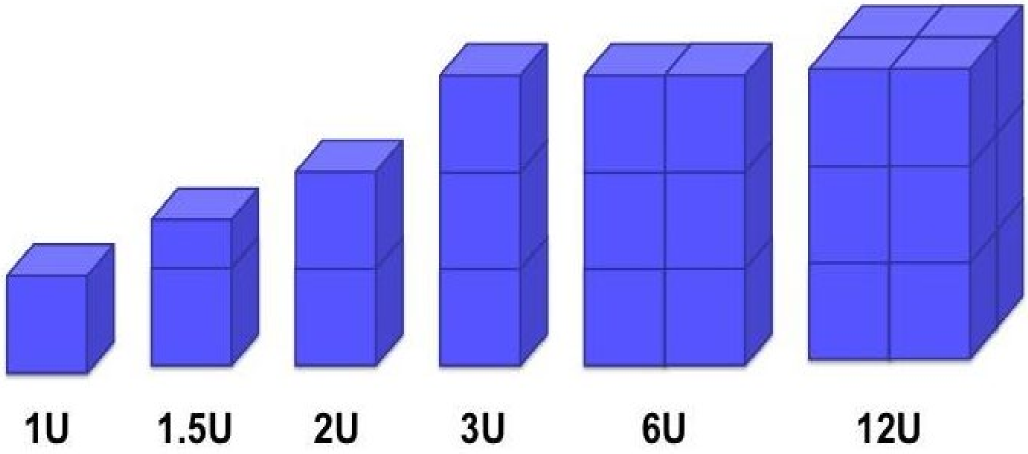

Figure 6. CubeSat configuration. Source: [6].

Compact satellites offer swift replacement in case of malfunctions, a feature that is both cost-effective and crucial during emergencies when time constraints prevent the construction and deployment of large, conventional satellites or constellations [9]. In satellite-based imaging systems, the failure of a single unit can jeopardize the entire mission. However, the flexibility of nanosatellites allows for prompt substitution of a malfunctioning satellite [9]. Through rideshare programs, a replacement nanosatellite can quickly secure a spot on an upcoming launch, ensuring minimal disruption to the constellation's operations and consistent coverage. This adaptability, affordability, and rapid production make small satellites a resilient and efficient solution for modern space missions [9].

C. SPARSE APERTURE ARCHITECTURE

Considering the Golay configuration, it is essential to examine the concept of a sparse aperture architecture. The fundamental principle behind sparse apertures is to use an array of smaller, individual collectors to fill the role of a single, large mirror [4]. NASA JPL explored three distinct control architectures for a sparse aperture formation. As illustrated in Figure 7, Architecture A showcases a singular spacecraft equipped with a deployable truss structure, designed to hold multiple collectors in orbit [4]. This architecture has the capability of producing a full optical image of a scene on the ground. It requires less fuel and a simpler control system compared to the other two architectures. However, due to the truss structure, this formation undergoes significant thermo-mechanical conditions and vibrations [4]. Architecture B suggests a tri-satellite system, comprising one combiner spacecraft and two collector satellites, specifically for star imaging. Architecture C mirrors Architecture B but is tailored for Earth observation [4]. Both architectures require a complex formation control system to maintain proper positions for accurate image collection.

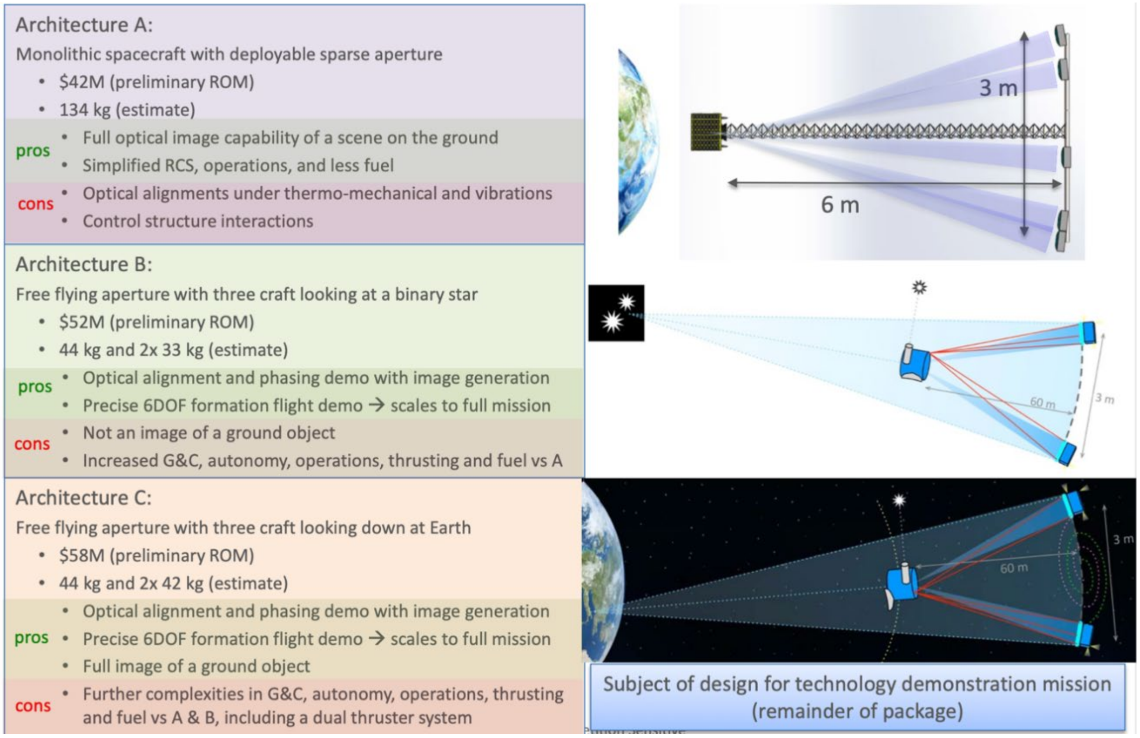

Architecture A:
Monolithic spacecraft with deployable sparse aperture
- $42M (preliminary ROM)
- 134 kg (estimate)

pros
- Full optical image capability of a scene on the ground
- Simplified RCS, operations, and less fuel

cons
- Optical alignments under thermo-mechanical and vibrations
- Control structure interactions

Architecture B:
Free flying aperture with three craft looking at a binary star
- $52M (preliminary ROM)
- 44 kg and 2x 33 kg (estimate)

pros
- Optical alignment and phasing demo with image generation
- Precise 6DOF formation flight demo → scales to full mission

cons
- Not an image of a ground object
- Increased G&C, autonomy, operations, thrusting and fuel vs A

Architecture C:
Free flying aperture with three craft looking down at Earth
- $58M (preliminary ROM)
- 44 kg and 2x 42 kg (estimate)

pros
- Optical alignment and phasing demo with image generation
- Precise 6DOF formation flight demo → scales to full mission
- Full image of a ground object

cons
- Further complexities in G&C, autonomy, operations, thrusting and fuel vs A & B, including a dual thruster system

Subject of design for technology demonstration mission (remainder of package)

Figure 7. NASA JPL sparse aperture formation architectures. Source: [4].

D. SPARSE APERTURE FORMATION FLYING

Among the three architectures presented in the NASA study, formation flying emerges as the most suitable choice for this research. Architecture A employs a truss structure that demands significant space and mass. This goes against the objective of seeking cost-effective solutions for a sparse aperture system. Additionally, employing a tangible structure like a truss in space necessitates addressing challenges related to size, vibrations, and the need for machine tolerance [4].

Formation flying is the best architecture to approach this problem. A group of small satellites would fly in formation with each satellite acting independently as a collector. One approach to create a satellite formation is to ensure all satellites share the same semi-major axis value [4]. By doing so, the collector satellites maintain their relative positions with the primary, or mother satellite combiner. Such an arrangement results in a cyclical orbit with minimal need for velocity adjustments. Figure 8 illustrates the cyclical movement of a satellite formation across different orbital inclinations [4].

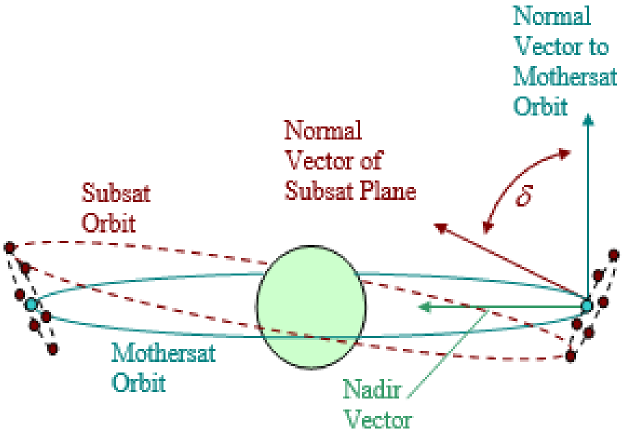

Figure 8. Orbit satellite formation. Source: [4].

In 2013, NASA JPL conducted a study on the formation flying of sparse apertures at MEO [10]. The research evaluated three distinct architectures for a system comprising six collector satellites. Each proposed method presented its own set of benefits and challenges [10]. The first architecture is the Leader/Follower (L/F) flight pattern, as illustrated in Figure 9. It is structured such that follower satellites consistently maintain their positions relative to a designated leader satellite. This approach is rooted in a hierarchical system theory, ensuring formation stability. It is adept at swiftly adapting to any variations in the flight trajectory. This L/F architecture has been chosen for the simulation segment of this thesis [10].

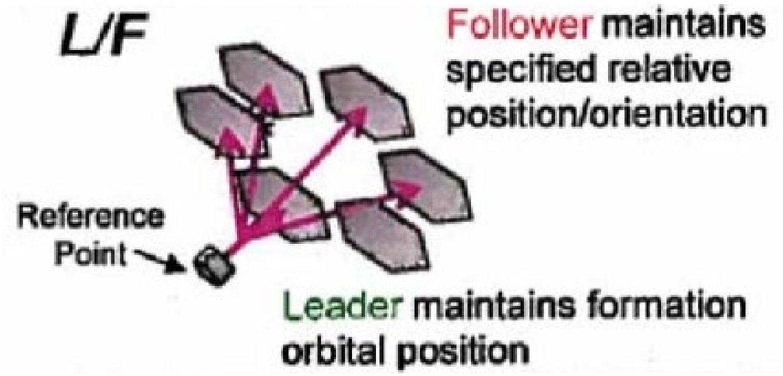

Figure 9. Leader/Follower (L/F) architecture. Source: [10].

The second architecture, termed the Center of Formation (COF) pattern, is illustrated in Figure 10. In this design, a reference point is determined based on the geometric center of the formation, or potentially a mass or fuel-weighted center [10]. While the COF approach offers better fuel efficiency compared to the L/F method, it lacks stability. Additionally, it necessitates a sophisticated control design and rigorous validation [10].

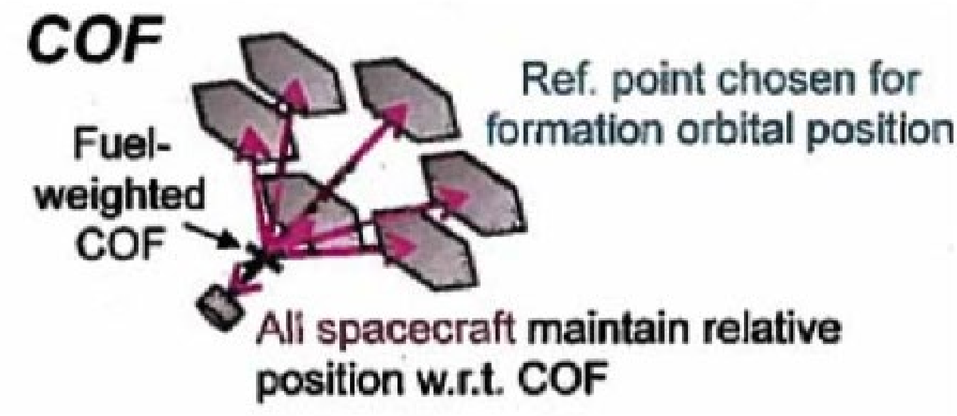

Figure 10. Center of Formation (COF) architecture. Source: [10].

The last flight architecture, depicted in Figure 11, combines elements from both the L/F and COF designs [10]. Initially, the main segments follow the COF approach, maintaining their positions relative to the formation's geometric center. Simultaneously, the instrument spacecraft, termed the "leader," employs the L/F methodology, acting as a "follower spacecraft" to bolster the formation's stability and coordination [10].

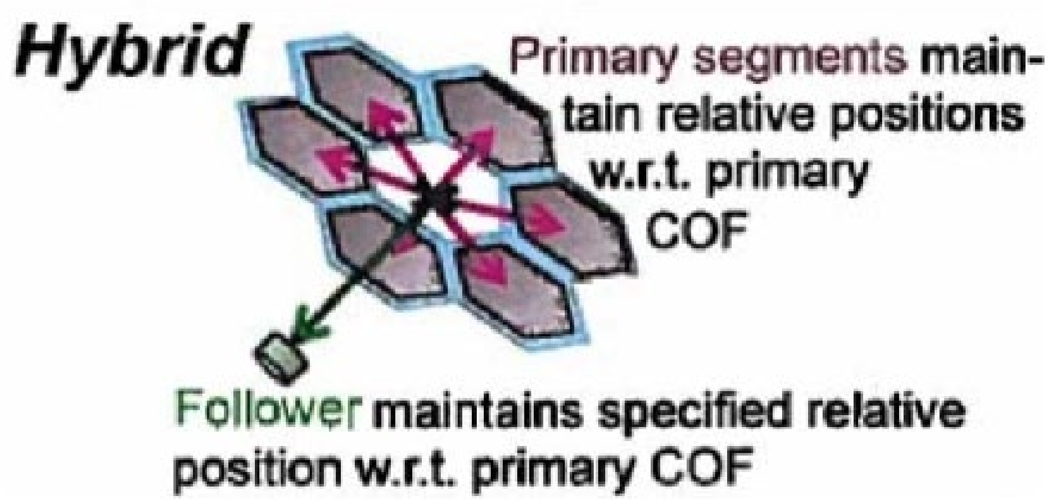

Figure 11. Hybrid L/F and COF architecture. Source: [10].

The study also focused on the optimal reference points for spacecraft formations. Central to their findings was the decision to set the combiner as the primary reference point for the formation [10]. This choice was made to simplify the process of measuring relative positions of the spacecrafts and to ensure a stable inertial reference, even if it meant potentially using more fuel. JPL's study also highlighted the continuous need for thrusting maneuvers for the spacecrafts in the formation [10]. Relying solely on natural orbital motion was not feasible; constant adjustments were necessary to maintain their positions. Three distinct orbital reference frames, illustrated in Figure 12, were proposed to guide these spacecraft maneuvers [10].

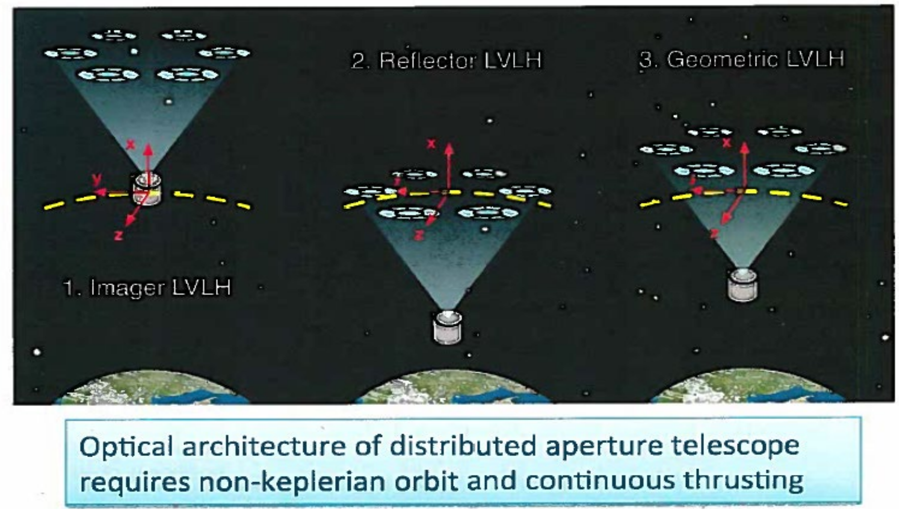

Optical architecture of distributed aperture telescope requires non-keplerian orbit and continuous thrusting

Figure 12. Formation orbital reference point. Source: [10].

This study assumes the formation to operate in MEO with a requirement of 10’s of mN thrust to maintain relative attitude control [10]. Furthermore, the design accounted for environmental factors such as gravity gradient and solar pressure. As can be observed in Figure 13, the environmental factors that had the greatest impact were gravity gradient and solar pressure.

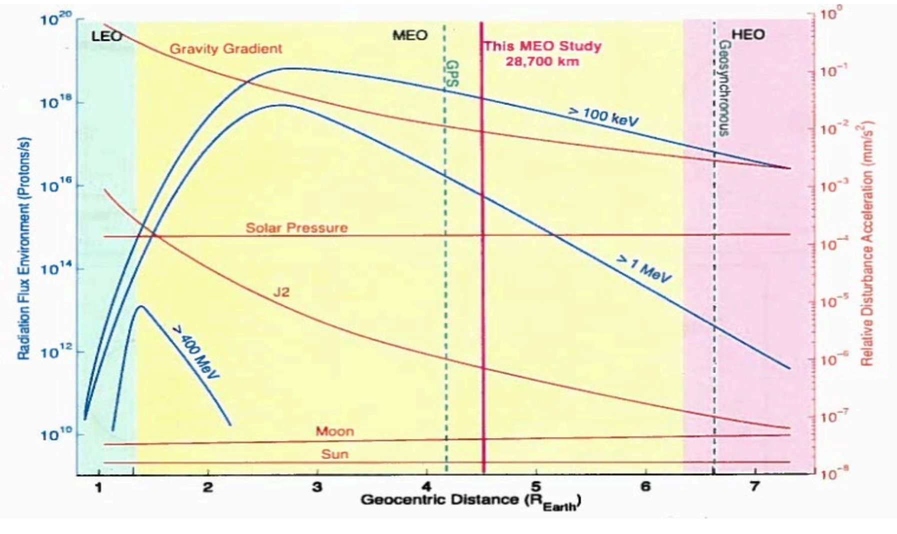

Figure 13. MEO disturbances. Source: [10].

Environmental disturbances and challenges in formation control can lead to aberrations in a sparse aperture system. These aberrations manifest as positional deviations in the mirror's x, y, and z axes, as shown in Figure 14 [10]. In a LF configuration, the follower satellite often undergoes rotational shifts across all three axes. There are also attitude errors in the x, y, and z axes that indicate translational discrepancies in its distance relative to the leader satellite [10].

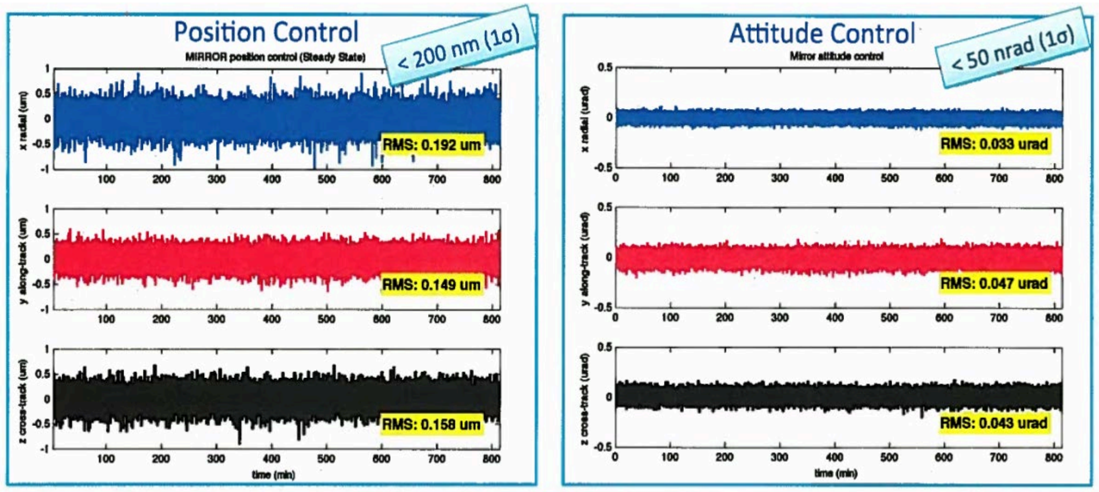

Figure 14. L/F formation control performance. Source: [10].

In real-world scenarios, sparse aperture systems face challenges due to environmental disturbances and the inherent complexities of formation control. These challenges manifest as aberrations in both the position and orientation of the system. On a testbed, these translational and rotational motions are simulated by introducing specific phasing and alignment errors, namely piston and tip/tilt, to one or more subapertures [5]. The goal is to emulate the resolution degradation a sparse aperture might experience in space. Specifically, rotational motion impacts the tip and tilt of the aperture, while translational motion influences the piston, or the forward and backward motion [5]. Two critical beam combining errors—piston error and tip/tilt error—must be maintained within specific tolerances for effective phased beam combining in a sparse interferometric array [5]. Piston error, resulting from optical path differences (OPD) along the Z-axis, is crucial when combining multiple beams. Any misalignment in OPD between sub-apertures can compromise the point spread function (PSF) quality. On the other hand, tip/tilt error, stemming from rotations in the X and Y axes, can also significantly affect the PSF [5].

Figure 15 depicts the impact of piston discrepancies on PSF, within an optical setup, based on findings from the MIT Golay-3 array study. Initially, when the OPD is zero, the PSF is sharp and intense in the center [11]. With an increase in piston error, the principal characteristic of the PSF moves in alignment with the direction of the error. Additionally, even a slight piston error can lead to a reduction in the PSF's peak intensity, affecting the overall image clarity [11]. As the OPD reaches 1.0λ in the figure, the PSF's width broadens, indicating a potential decrease in the system's resolution or ability to distinguish fine details [11].

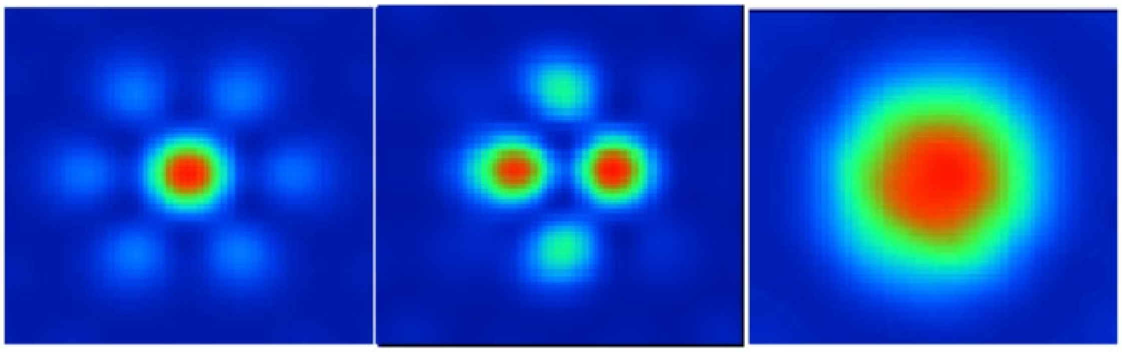

PSF plot of Golay-3 array from left to right with zero OPD, 0.5 λ OPD, and 1.0 λ OPD; Tilt error.

Figure 15. PSF plot of Golay-3 array. Source: [11].

E. CHALLENGES TO SPARSE APERTURE SYSTEMS

The biggest challenge facing a sparse aperture system is the need for exact formation flight control. The satellite formation will require a metrology system, the science of measurement and its application, that has a high degree of measuring precision. [12]. Each satellite in the formation demands this precision to measure distances between its counterparts. Any deviation from this precise alignment can cause interference in the combined light from the satellites, resulting in images with diminished resolution. Beyond mere distance, the angular position or orientation of each satellite's mirror is equally critical. Minor angular misalignments can significantly compromise the quality of combined images. Additionally, external factors like vibrations, jitters, and environmental disturbances can further disrupt a satellite's position and orientation.

Recognizing these challenges, NASA JPL proposed a laser metrology system capable of nanometer-level precision measurements [10]. This system would transmit laser beams between satellites, offering real-time position tracking for each component in the constellation [10]. Central to this proposal is the OPTIIX Laser Metrology system seen in Figure 16 [10]. The OPTIIX system employs Laser Metrology-based control (MET) to consistently maintain the alignment of the telescope optics. It monitors positional changes in both primary and secondary satellites. This monitoring is facilitated by the Laser Distance Gauge (LDG), which uses lasers to measure distances [10]. These LDGs, when networked together, form the "Laser Truss." This truss measures the primary mirror in relation to the secondary mirrors. Furthermore, the Wavefront Sensor and Control (WFS&C) within the OPTIIX system is designed to determine and maintain the optimal alignment of the telescope optics [10]. With the data from the Laser Truss network, the system can achieve continuous alignment control, boasting a bandwidth of less than 10 Hz and maintaining a wavefront error below 20 nm [10].

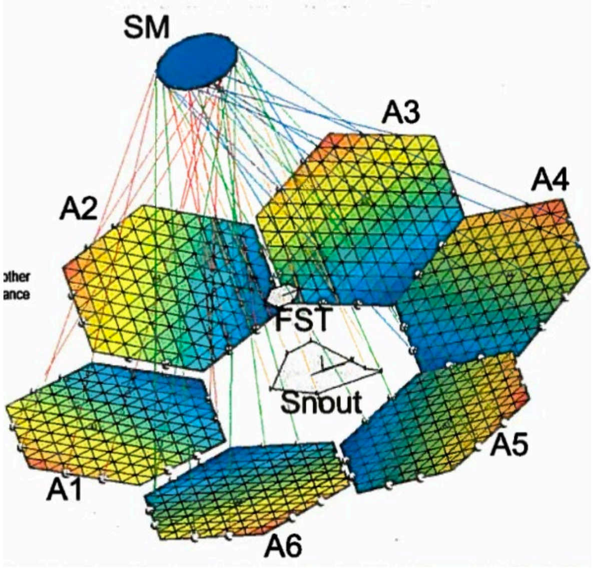

Figure 16. OPTIIX laser metrology system. Source: [10].

F. PREVIOUS AND CURRENT RELATED SPARSE APERTURE PROJECTS

There are many other studies in the field of sparse aperture that are being conducted. The Major Science and Technology Projects in Sichuan Province developed a Golay3 sparse-aperture system, as depicted in Figure 17 [13]. This system employs a specific arrangement of sub-apertures to achieve enhanced imaging capabilities [13].

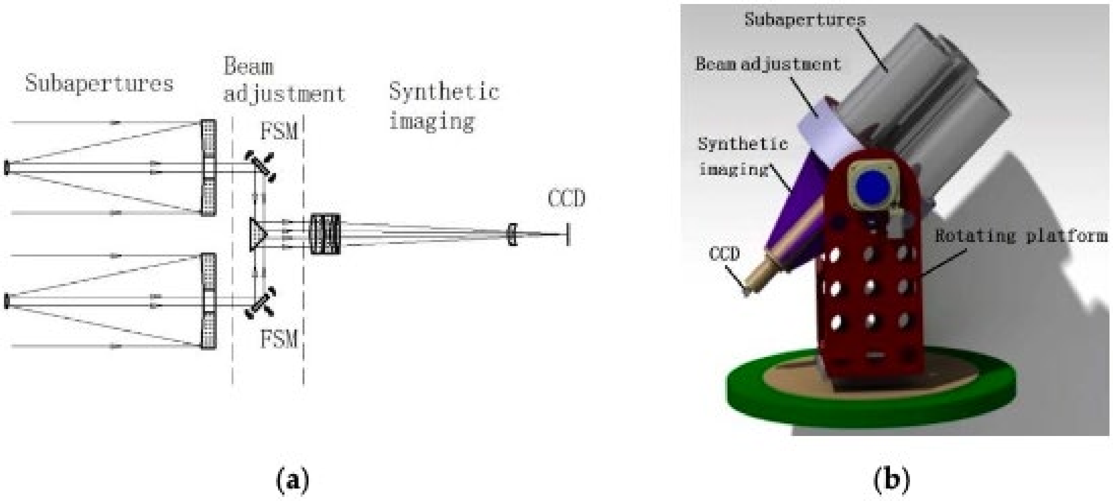

(a) side view of the light path structure; (b) three-dimensional model.

Figure 17. Golay3 system. Source: [13].

The system works by capturing light through multiple small subapertures [13]. These subapertures work together to create clear, high-resolution images, like those produced by larger, single-aperture systems [13]. A significant challenge in this system is the “cophasing error,” which results from positional discrepancies between the subapertures, causing phase variations in the beams. As illustrated in Figure 17a, positional errors between the subapertures can lead to different beam phases [13]. This error can degrade the imaging quality if not adequately managed. The system’s design incorporates both rough and precision adjustments for beam steering. The rough adjustment provides a broad adjustment range, while the precision adjustment addresses the “cophasing error.” In the testing phase, the system uses a large-diameter collimation to simulate an infinite point target, with a Charge-Coupled Device (CCD) image surface as the detection object. Adjusting the system allows the beams from the three subapertures to converge and interfere on the imaging plane, producing an image of high resolution. [13].

However, the Golay3 system has limitations. It does not accurately simulate three space apertures, and its testing lacks real-world environmental conditions or genuine satellite orbit simulations. This makes its evaluations more of an idealized test case, with perfect environmental conditions, and no disturbances. The system also depends solely on sparse aperture adjustments for corrections, without a separate controlling satellite like in a L/F architecture. Consequently, its suitability for actual space missions is yet to be determined.

Another study is the MIT Adaptive Reconnaissance Golay-3 Optical Satellite (ARGOS) project. The ARGOS project, as shown in Figure 18, is the first sparse aperture array testbed that replicates the operations of an imaging observatory in a terrestrial setting with the influence of gravity (1-g) [1].

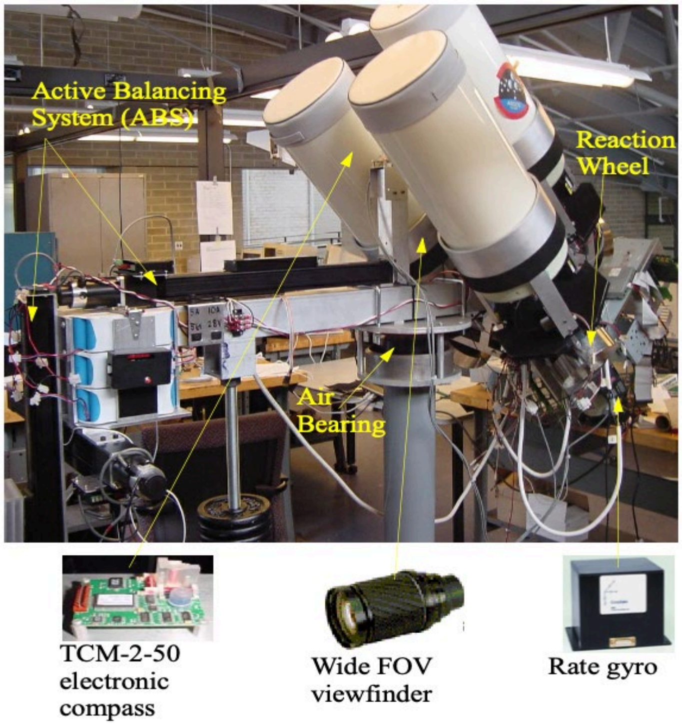

Figure 18. Final ARGOS system configuration. Source: [1].

The ARGOS system employs Fizeau interferometers, which are adept at generating direct imagery with uniform u-v coverage, making them particularly effective for imaging large-scale scenes and rapidly moving objects [1]. The system's design incorporates three apertures set in a Golay-3 pattern, funneling light to a central hub and subsequently to a CCD. Real-time optical adjustments are facilitated through wavefront sensing techniques to counter initial alignment discrepancies [1]. The resulting image quality is on par with that from a single-aperture telescope. The ARGOS setup is engineered to tackle practical issues like the vibrational impact on spacecraft structures and wavefront distortions within the system [1]. Despite its advanced design, the system's coherent beam combining has yet to produce a phased image of an actual celestial target due to existing technical hurdles [1].

At the Naval Postgraduate School, Sean Sundey conducted a study that focused on the development of a laboratory testbed, shown in Figure 19, to simulate sparse aperture formations [4]. This research was centered around creating an optical testbed designed to simulate the relative movements of satellites in a formation collector system [4]. The setup used two sparse aperture collector mirrors to replicate potential disturbances satellites in formation might encounter while in formation [4]. A key component of this study was the use of a 6-Degree of Freedom (DOF) stage. When used with tools such as MATLAB and Spatial Analyzer software, it allowed for precise generation of simulation data points for formation flying. The integration of the FARO Laser Tracker in this research highlighted the role of laser interferometry in tracking and reporting formation positions and error. Additionally, the research verified the interference fringe patterns of collector mirror positions, emphasizing the accuracy of computer modeling in this area [4].

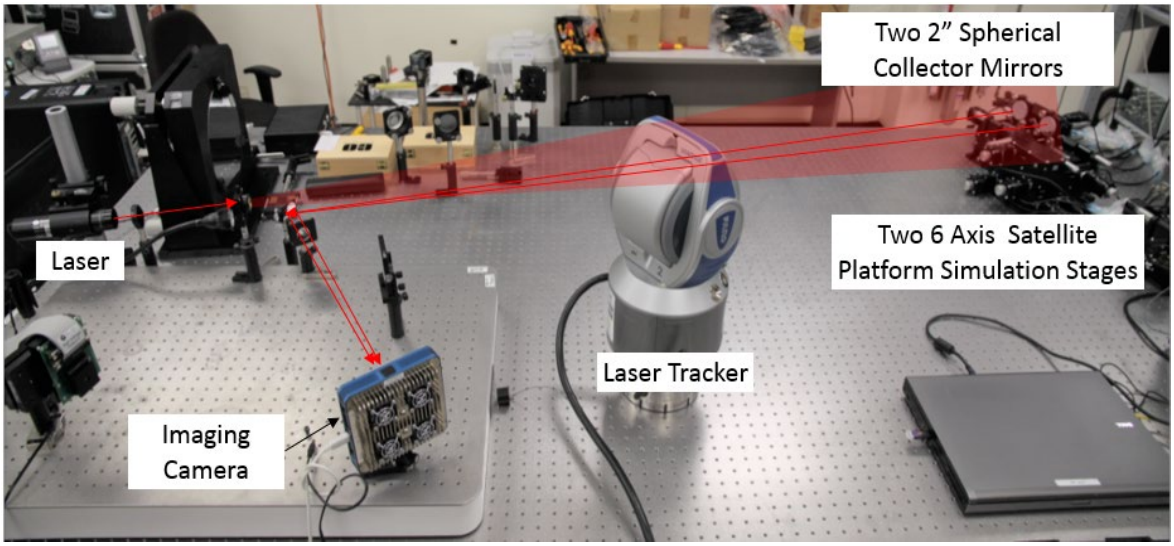

Figure 19. Two collector mirror testbed design. Source: [4].

Sundey’s research helped lay the foundation for the three-collector mirror testbed design here at NPS. He identified certain areas that required further exploration such as the metrology system [4]. There was a clear indication that greater precision was necessary, especially as the industry moves towards utilizing shorter light wavelengths [4]. The study also discussed the idea of expanding to a three-mirror system and looking into the merits and challenges of using parabolic, spherical, and flat mirrors [4]. Another area for exploration was to develop a real-time, closed-loop control system, with an emphasis on the need for dynamic control algorithms capable of reacting to instantaneous metrology data [4]. Additionally, the challenges faced in computer modeling during this study highlighted the need for enhanced simulation tools. In retrospect, Sundey’s research provided valuable insights into the optical sparse aperture domain and set the direction for future research, highlighting areas that need further innovation and refinement [4].

THIS PAGE INTENTIONALLY LEFT BLANK

III. EXPERIMENTAL SETUP

This chapter presents a detailed overview of the NPS Sparse Aperture Testbed, outlining its key components and functionalities. It also addresses the practical aspects of the testbed's implementation and the challenges faced in simulating the complexities of satellite formation flying in a laboratory setting.

A. NPS SPARSE APERTURE TESTBED OVERVIEW

The sparse aperture concept has been demonstrated in parts but not in an integrated form. A laboratory testbed has been developed at NPS to demonstrate the integrated sparse aperture system concept. The testbed incorporates fundamental system components such as a formation flying satellite platform, high precision metrology, and an alignment and phasing system that are required for coherent light combination. The goal of this testbed is to provide real time data on image collection and distortion for a simulated satellite formation concept [14].

In the sparse aperture testbed shown in Figure 20 a white light source, illuminated or reflected off an USAF resolution test, is collimated by a 0.25 m parabola and sent to three 0.05 m sparse spherical mirror array on separate 6 axis motion stages. These stages represent a small satellite platform where satellite formation motion is simulated. Each mirror on the stage, simulates an individual collector craft. The fine adjustments of the 6-DOF simulator on the stage will provide micron level disturbances to the formation alignment [14]. To measure the motion of the sparse aperture, a laser metrology system consisting of nine (9) single-axis displacement interferometer was employed in the testbed. The laser interferometer probes the displacement of three corners of each 0.05 m diameter spherical collector mirrors [14].

The stage labeled A on Figure 20 is the collector spacecraft or the leader spacecraft in the L/F architecture. Light from collector mirrors is optically relayed to the combiner platform, where each beam is reflected off a 0.02 m diameter flat mirror mounted on a tip/tilt/piston stage to correct the aberration caused by satellite formation motion. The coherently combined light is then reflected to a CCD imaging camera for analysis [14].

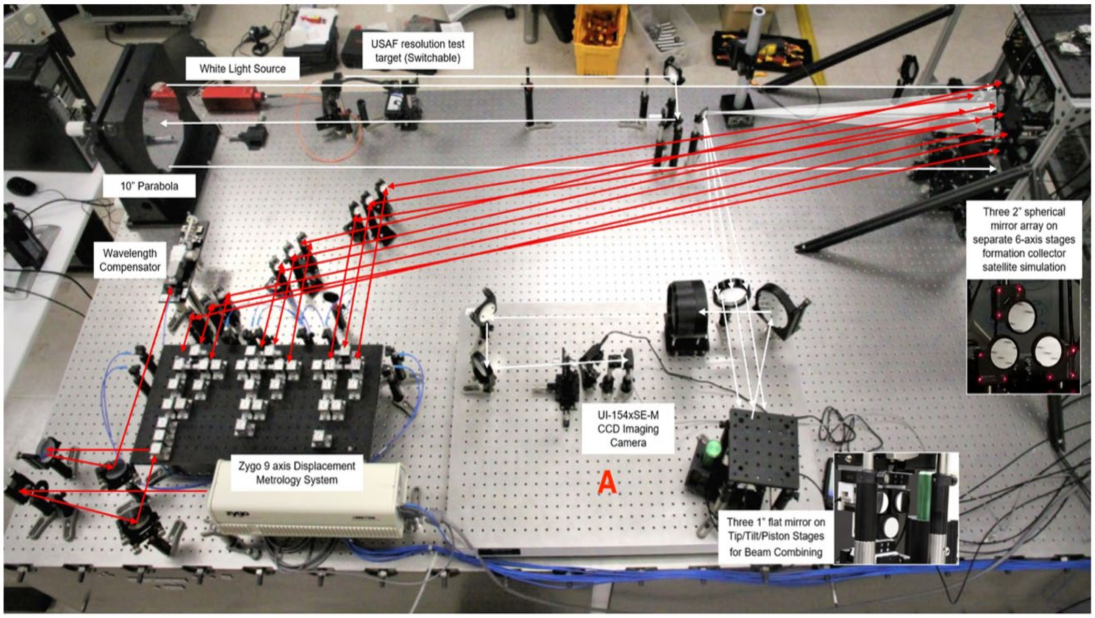

Figure 20. Three-mirror design testbed. Source: [14].

B. TESTBED COMPONENTS

This chapter provides the technical background for the different components of the testbed: (1) Newport RS Table (2) light point source and scene image, (3) NanoMaxTM NanoPositioning Flexure Stages, (4) Optics Mirrors, (5) Laser Metrology System, (6) Combiner Spacecraft Platform, and the (7) Image Development System (IDS) camera. This testbed will focus on introducing error into the collection process for each collector and then correcting the error through control software.

1. Newport RS Table

The Newport RS seismically isolated table, Figure 21, is the basic testbed for the optical bench installed in the Spacecraft Research and Design Center (SRDC) laboratory at NPS. The table sits on six precision tuned dampers which eliminate resonance with the surrounding environment. This ensures the optical path is free of external disturbances. The overall dimensions for the table are 1.498 m x 3.048 m x 0.610 m and weigh 1360 kg [4].

Figure 21. Newport RS seismically isolated table. Source: [15].

2. Light Point Source and Scene Image

In this experiment, three primary light source and image tools were chosen: a JDS Uniphase laser emitter, a panchromatic white light source, and a United States Air Force (USAF) Resolution Test Target. The laser emitter emits a monochromatic light at a wavelength of 632.8 nm [4]. This specific wavelength simplifies the calibration and alignment of the mirrors, especially before proceeding to tests involving a panchromatic light. The panchromatic light source, which emits light across a broad spectrum, is essential for observing the interference patterns and fringes produced when the three collector beams converge. To evaluate the system's imaging capabilities, the United States Air Force Resolution Test Target is used. As depicted in Figure 22, this target contains intricate patterns that allow for the assessment of the system's resolution. The area of interest, highlighted by the red box, is the specific section that the mirrors aim to capture and analyze. For the scope of this thesis, measurements were primarily focused on the panchromatic light source.

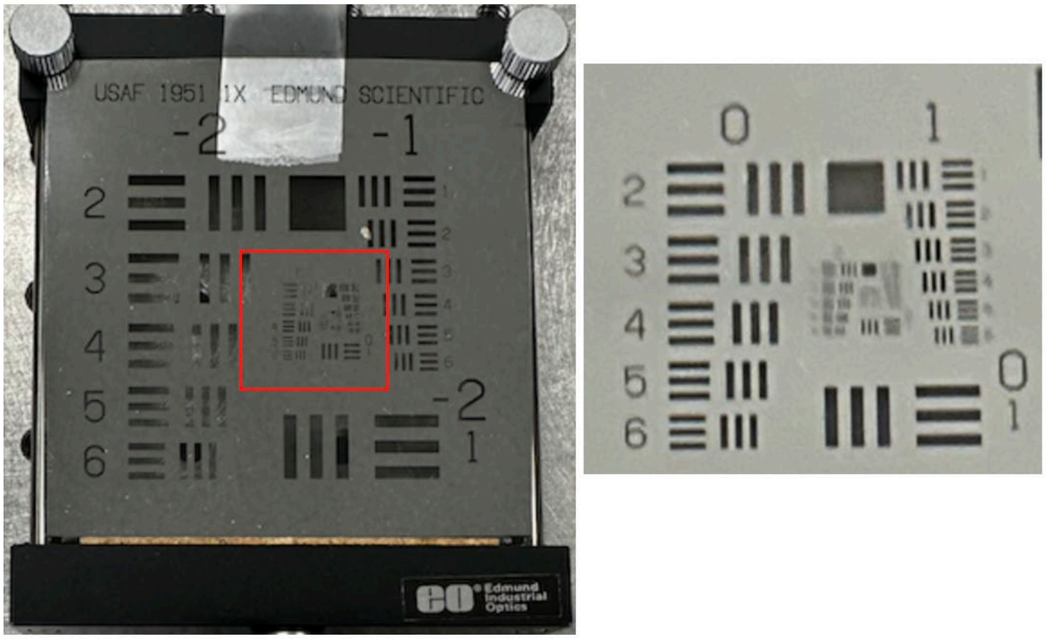

Figure 22. USAF resolution test target.

3. ThorLabs Nanomax 600 Series 6-DOF Simulator

Three collector mirrors, representing the sparse apertures, were affixed to 6-DOF motion simulation devices. These devices simulate the inherent motion errors that satellites might experience during formation flying. For this study, three 6-axis NanoMax NanoPositioning Flexure Stages from ThorLabs were employed as the motion simulators. These stages are designed to offer 4 mm of travel across each primary axis and can accommodate six degrees of motion in pitch, roll, and yaw [16]. Figure 23 showcases the three 6-DOF simulators, each with a collector mirror securely mounted on its top surface.

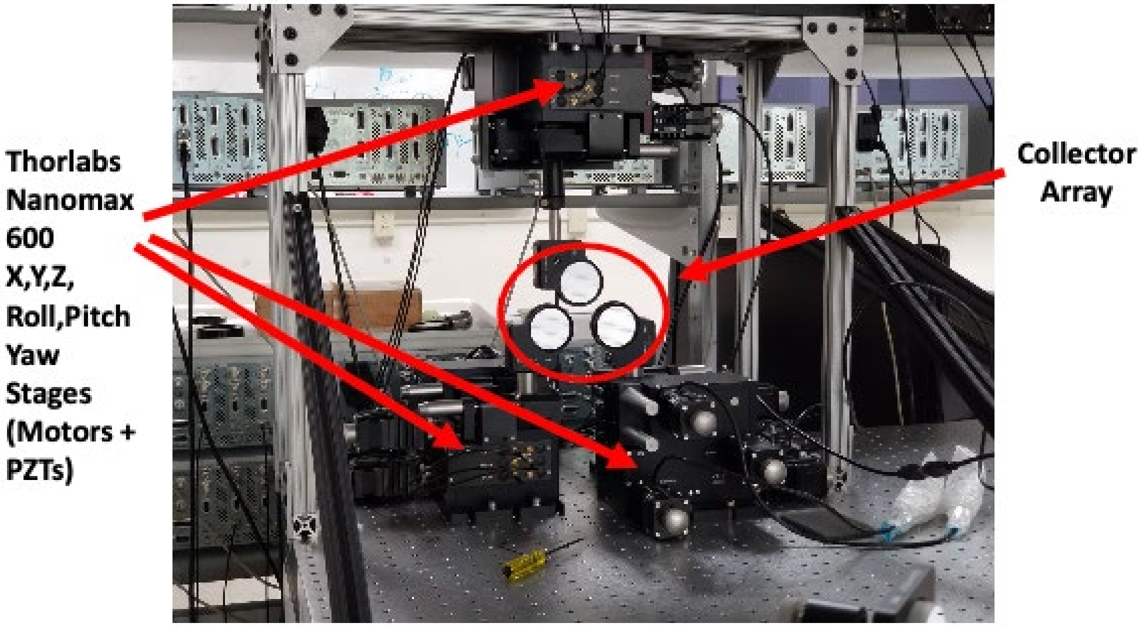

Figure 23. Thorlabs 6-DOF motion simulators. Source: [17].

For course and fine tune adjustments, electronic piezo controllers control the three motion simulators. These controllers, manufactured by Thorlabs, have a 75 V range with <3 mV-RMS errors and are used to adjust the travel of each degree of freedom for each stage [18]. A program in MATLAB 2016A and Advanced Positioning Technology (APT) software provided by Thorlabs allow simultaneous control of all controllers in all degrees of freedom through a computer interface.

4. Optics Mirrors

The lens and mirror components used in the design of the test bed were all provided by Edmunds Optics. The primary collector mirrors are spherical mirrors with f/20 curvature. Each collector contains a single mirror mounted on an adjustable bracket that is mounted on a DOF simulator. Each mirror is designed to be 50.8 mm in diameter. It is coated with enhanced aluminum metal that has a wavelength range of 450 to 650 nm [17].

Figure 24 shows the Golay-3 configuration design of the sparse aperture array for the NPS testbed. This design was selected because all three mirrors are equi-distant from the center to create an effective overall diameter of 127 mm. This keeps spherical aberration to less than or equal to 0.25 of a wavelength. Furthermore, this design is optimal for non-redundant distances and angles which improves imaging with the three collector mirrors [17].

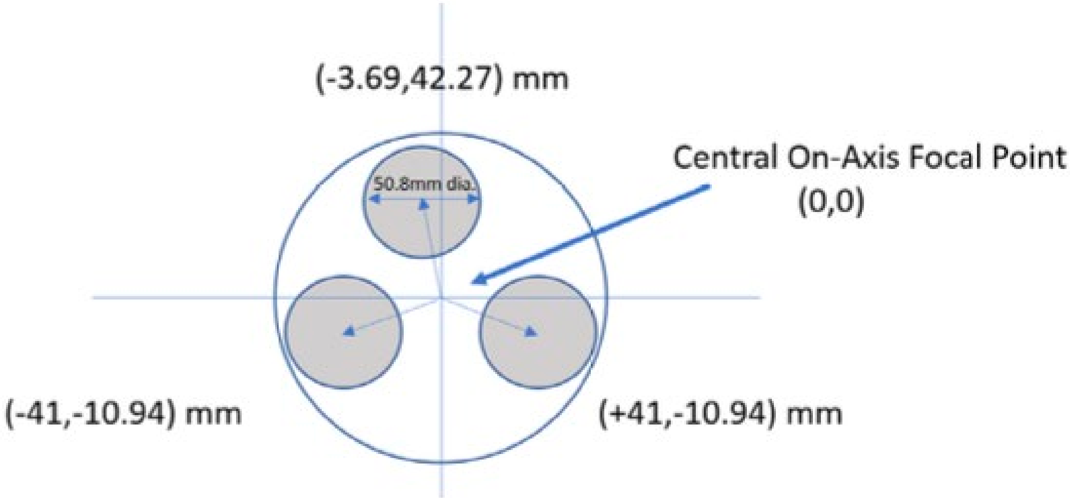

Figure 24. Sparse aperture array design. Source: [14].

Each collector mirror is equipped with three corner cubes, as depicted in Figure 25. These corner cubes play a critical role in the laser metrology system, which is further elaborated upon in the laser metrology system section. Their primary function is to assist in measuring drift within the metrology system. The cubes will be identified as the position they hold on the collector mirror for further analysis in the experimental section.

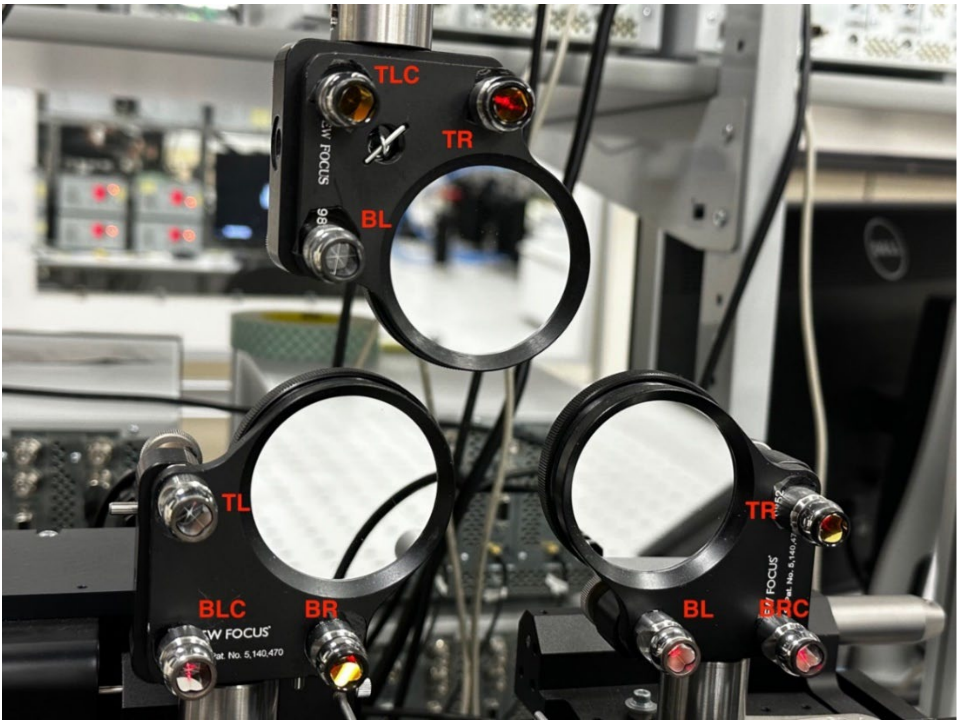

Figure 25. Corner cubes on collector mirror.

Spherical mirrors are the preferred choice for the sparse aperture array due to their inherent advantages over parabolic mirrors. One of the primary benefits is that spherical mirrors enable all collector sparse apertures to possess a mirror surface of consistent shape. This uniformity simplifies optical path corrections as coherent light combination necessitates only three degrees of freedom (tip, tilt, and piston) for adjustments. Also, when a sparse aperture system has distinct platforms for beam collection and beam combination, it permits the use of spherical mirrors with extended focal lengths. This eliminates the need for spherical aberration correctors, ensuring the optical system achieves diffraction-limited performance [17].

To emulate an image appearing at an infinite distance, a large parabolic mirror, 254 mm in diameter, shown in Figure 26, is utilized. This mirror reflects and collimates an image projected onto it. The reflection from the parabolic mirror serves as a simulation of a distant target, much like observations made by long-range satellites. This setup facilitates the projection of images onto the collectors, enabling a visual reconstruction from the combiner to be achieved [14].

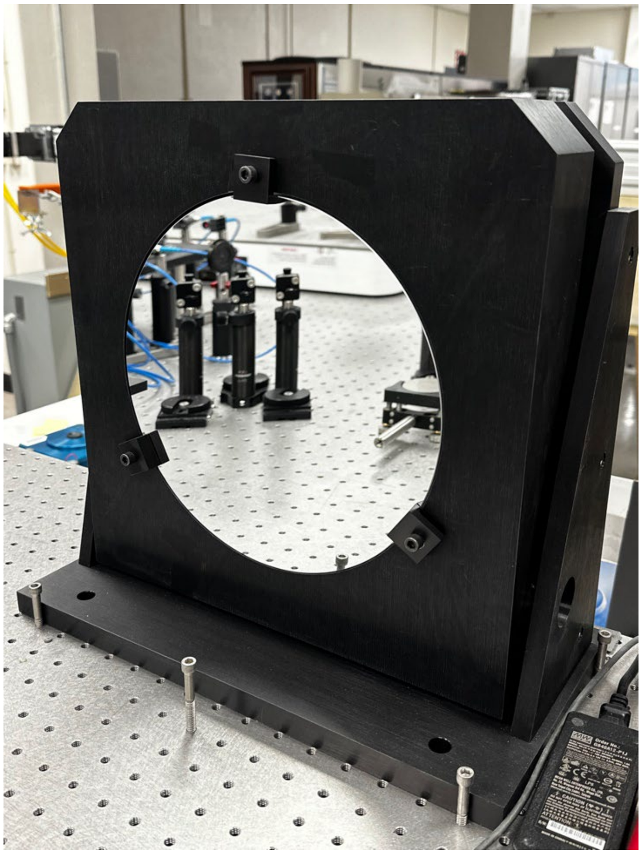

Figure 26. Sparse aperture testbed parabolic mirror.

5. Laser Metrology System

To measure the movement of the sparse apertures, a sophisticated laser metrology system was incorporated into the testbed, seen in Figure 27. This system is composed of nine single-axis displacement interferometers. Each interferometer is designed to measure the displacements of three corner cubes mounted on each 0.05 m diameter spherical collector mirror. The core components of this metrology system include the ZYGO ZMI laser, plane mirror interferometers, a wavelength compensator, and a range of supplementary accessories such as standard fold mirrors, beam splitters, and fiber optic pickups and cables to ensure flexible configuration.

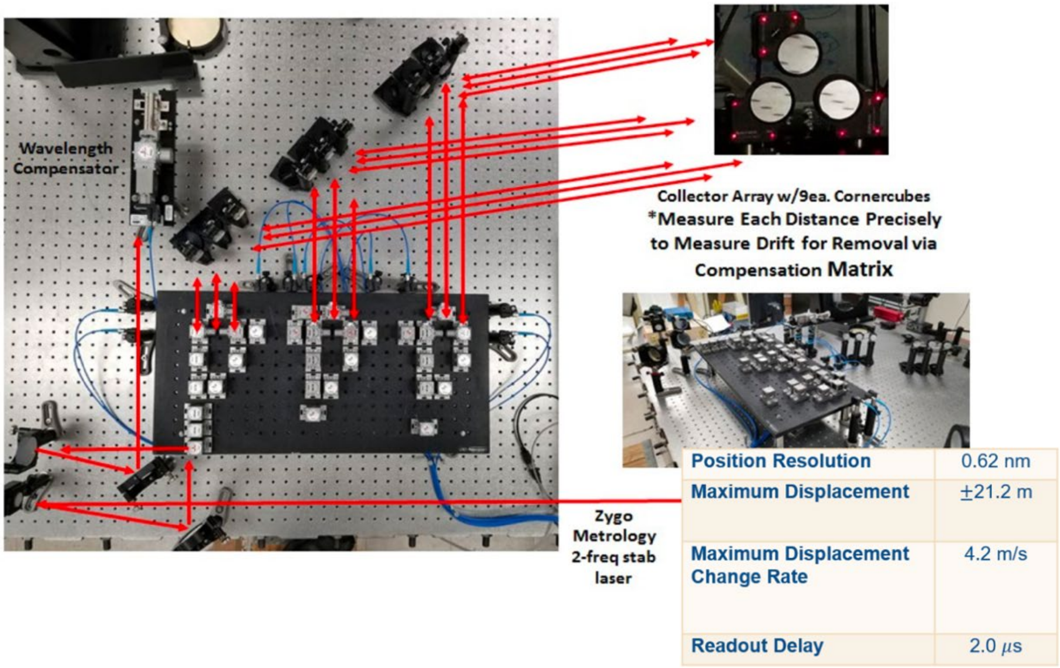

Position Resolution	0.62 nm
Maximum Displacement	±21.2 m
Maximum Displacement Change Rate	4.2 m/s
Readout Delay	2.0 μs

Figure 27. Laser metrology system for NPS testbed. Source: [14].

The ZMI 7702 laser, a product of Zygo, is a state-of-the-art Helium-Neon, Continuous Wave, Two-Frequency, Linearly Polarized system designed for precision position metrology [19]. It emits a coherent beam of light with a frequency difference of 20 MHz ± 1600 Hz and a peak beam power output of 1 mW [19]. The laser's exceptional wavelength accuracy is maintained at ±0.002 ppm over a 24 hour period and ±0.02 ppm throughout its operational lifespan [19]. This laser directs its beam to a series of beam splitters, which then partition the beam into nine separate beams, each aimed at a set of three plane mirrors.

These beams are directed towards a set of three corner cubes on each spherical mirror, seen in Figure 25. Corner cubes, also termed retroreflectors, possess the distinctive capability of reflecting light directly back to its source, irrespective of the incoming angle. This characteristic renders them indispensable in high-precision optical systems [20]. Post-reflection, the beams return to the beam splitters, where they merge again. The laser interferometers then gauge the displacements of the collector mirrors by discerning the path length differences, which arise due to the movement of the spherical mirrors.

The Zygo laser tracker system provides a position resolution of 0.31 nm. This system has a position range of ± 10.6 m and utilizes a 36 bit, 2's complement position format [21]. The time stamp resolution is set at 25 ns, indicating its capability for high-frequency measurements [21]. The tracker can achieve a maximum velocity of 2.1 m/s and withstand a maximum acceleration of 100 g, with a limitation of 10 g during reset [21]. The electronic accuracy of the system is contingent upon velocity, with values of 1.2 LSB at ± 0.1 m/s, 1.4 LSB at ± 1.0 m/s, and 1.6 LSB at ± 2.1 m/s [21]. The data age, when output through P2, is typically 1 µs, and the data age uncertainty, when compensated, is ± 1.2 ns across three boards [21].

A MATLAB code, created by Jefferey T. Baker of Baker Adaptive Optics, enables the user interface with the laser tracker. This code, detailed in Appendix A, interfaces with the laser metrology system via an ethernet cable, collecting real-time data for each measurement. Using the gathered displacement measurements, a transformation matrix is formulated. This matrix delineates the correlation between the motions of the collector mirrors, as detected by the laser metrology system, and the necessary adjustments by the piston/tip/tilt stages. The laser interferometer employs this transformation matrix to convert raw tip, tilt, and piston measurements into the requisite corrections for the compensating mirrors.

6. Combiner Spacecraft Platform

Light from the collector mirrors is optically relayed to the combiner platform which plays the role of the leader spacecraft in the L/F formation. Each beam is reflected off a 0.02 m diameter flat mirror mounted on a tip/tilt/piston stage to correct the aberration caused by satellite formation motion. The array configuration is presented in Figure 28. There are two stages on top, one on bottom that are both coarse and fine adjustable. There is a minimum error edge gap on the left and right of about 10 mm and the top and bottom of about 5 mm. This layout makes a close 2:1 fit to the Collector Array to provide corrections to the collected light [17].

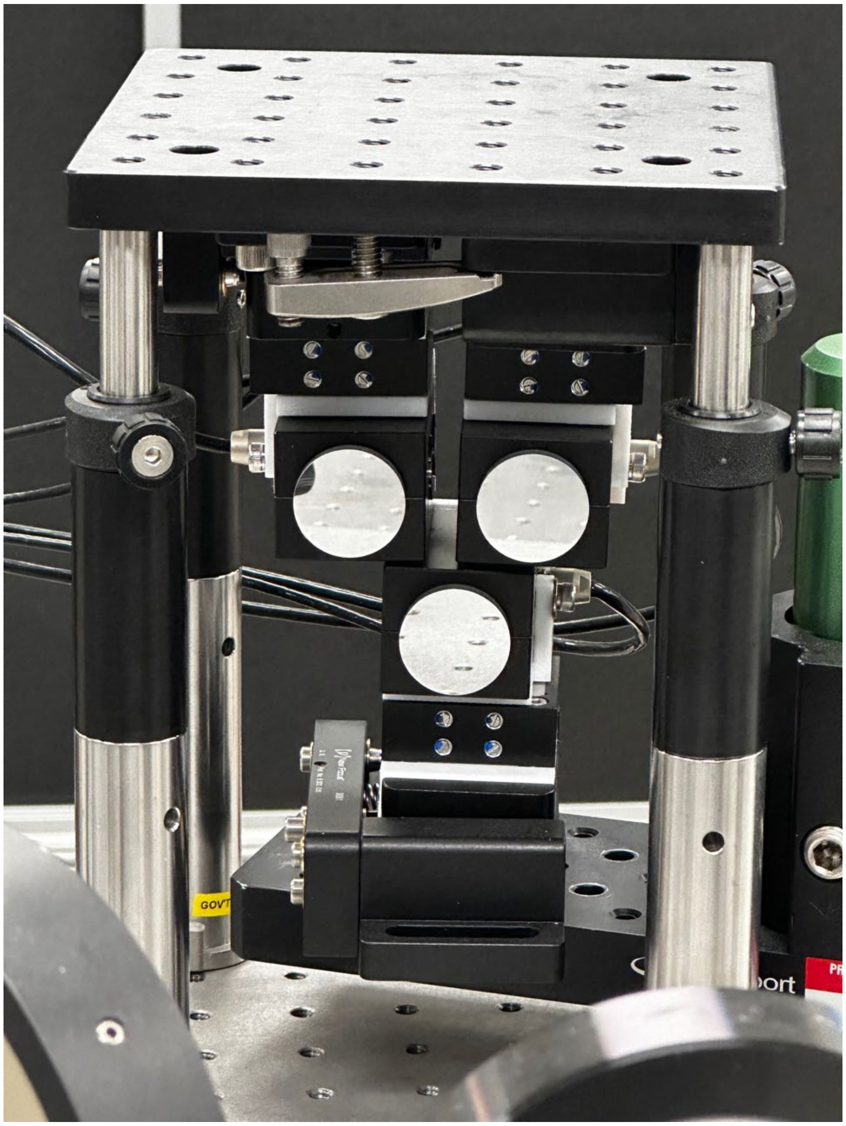

Figure 28. Combiner sparse array layout.

Each flat mirror is attached to a PI S-335SHM2 tip/tilt stage that is labeled A on Figure 29. The S-335 Piezo Tip/Tilt platform, developed by Physik Instrumente (PI), is advertised to have a tip/tilt angle to 35 mrad, with a high optical deflection angle to 70 mrad [22]. Each stage is then attached to the moving part of the PI P-621.1 ICD translation stage, labeled B on Figure 29. It is a piezo linear precision positioner that travels in the X, Y, Z plane in ranges from 50 to 1800 um [23].

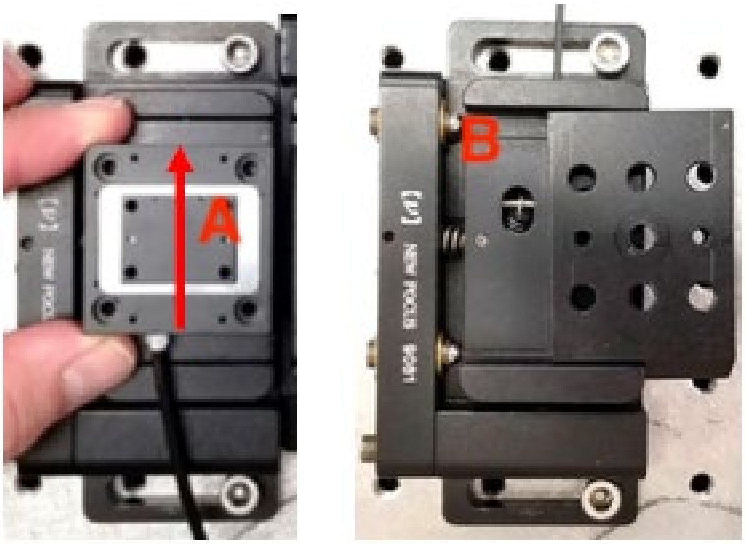

Figure 29. Combiner mirror stage. Source: [17].

The coherently combined light with the corrections is then fed through a series of lenses into the CCD imaging camera show in the red box in Figure 30.

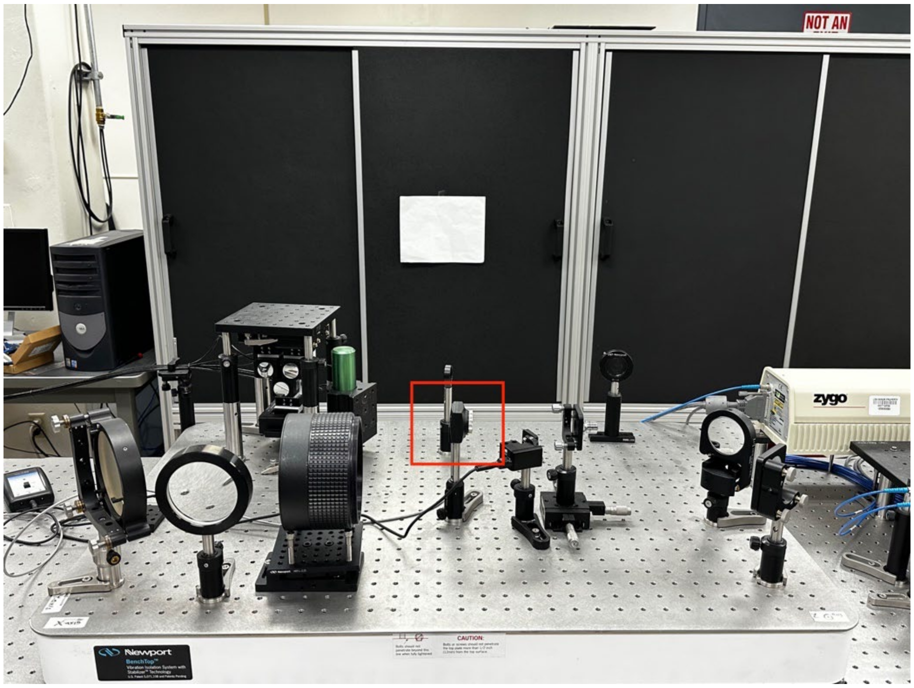

Figure 30. Combiner platform.

7. Imaging Development System (IDS) Digital Camera

The testbed employs the UI-1540LE-M-GL camera, a product of Imaging Development Systems. This camera is equipped with a monochrome sensor featuring a rolling shutter, known for its linear sensor characteristics [24]. With a resolution of 1.31 Mpx, it provides a 1280 x 1024 px focal plane array [24]. The camera's aspect ratio is 5:4, and it delivers images with a 10 bit ADC and an 8 bit color depth [24]. The optical sensor size has dimensions of 6.656 mm x 5.325 mm and a diagonal of 8.52 mm [24]. Each pixel on this sensor is 5.2 µm in size [24]. Notably, the camera can achieve a frame rate of twenty five in both free run and trigger modes [24]. The CCD focal plane of the camera serves as the focal point for the collector mirrors post-correction. The images captured by this camera are versatile and can be used for tasks ranging from aligning optical systems to observing the optical outcomes of beam interference.

C. TESTBED IMPLEMENTATION AND CHALLENGES

The comprehensive testbed, as illustrated in Figure 20 is designed to emulate the dynamics of a three-collector system following the L/F architecture. The camera, equipped with continuous video functionality, works in tandem with a MATLAB script to facilitate image capture and video recording for subsequent analysis. This script processes the data, presenting the imagery in grayscale, which aids operators in monitoring and fine-tuning the calibration. The primary focus during the image analysis is on fringe interference and intensity patterns.

The 6-DOF simulators introduce relative motion to the collectors, thereby injecting errors. This setup tests the ability of the laser metrology system and the combiner spacecraft to rectify these aberrations. The laser metrology system's role is pivotal as it gauges the displacement of the collector mirrors, supplying real-time orientation data. Leveraging this data, the combiner satellite platform makes the necessary optical corrections.

However, the testbed does come with its set of challenges. The current setting for the aperture piston motion peak on the correction stage is capped at 20 µm. This restriction does not fully represent the extensive range of translational motions that a satellite formation might experience in real-world scenarios.

THIS PAGE INTENTIONALLY LEFT BLANK

IV. METHODOLOGY FOR SIMULATION AND EXPERIMENT

The objective of the sparse aperture study is to determine if the combiner satellite can compensate for aberrations in the images or point light source gathered by the collector satellites. The simulation was subjected to two distinct error types to test the quality and accuracy of the compensator. The two types are random errors and errors derived the NASA JPL study.

The testbed is controlled by three distinct software programs housed on a single computer. A MATLAB code controls the Thorlabs 6-DOF units, the PIMikroMove 2.26.0.6 software operates the PI tip/tilt/piston platform on the combiner satellite platform, and the uEye Cockpit software operates the IDS camera. The MATLAB script, detailed in Appendix A, introduce errors and measure collector mirror displacements. Each operation session necessitates an initialization phase and meticulous alignment of the table.

The Zygo laser metrology system interfaces with five ZMI 2402 Displacement measurement boards that are housed within a VME Chassis. Each board has two axes of measurements which measures the displacement of the nine corner cubes on the collector mirrors. Each board provides sub-nanometer resolution to calculate displacement using optical signals from the interferometers [21] The VME Chassis communicates with the operating computer via an Aruba 2920–24G PoE + Switch, ensuring seamless data transfer.

The laser metrology system is controlled via MATLAB code and creates a transformation matrix of measurement profiles. The three corner cubes affixed to each collector bracket provides a reference plane for the position of a single collector mirror. Once each data point is located and measured initially with all collector mirrors aligned, reference points would be created for any change in the position of the mirror.

The Thorlabs 6-DOF simulators offer dual control mechanisms: manual adjustments via the piezo control units and software-based interventions. Integration with MATLAB was achieved through the APT software suite supplied by Thorlabs. To facilitate computerized control, each channel was meticulously mapped and designated. After initializing the MATLAB simulation, diverse scripts were developed to facilitate user-specified motion trajectories. Preliminary tests were centered on distinct voltage inputs to calibrate the system.

The operational voltage range for the piezo controller spanned from 0 to 75 V with each channel's readout precise to two decimal places. However, a consistent voltage variation of ±0.02 V was observed in a steady state across channels [4]. This variance, although persistent, was inconsistent across channels and could not be mitigated. Given its minuscule magnitude relative to the testbed's overall precision, this deviation was deemed inconsequential for experimental objectives [4]. For dynamic motion simulations, scripts were tailored to generate sinusoidal trajectories, influencing the movement of the collector. This approach was scalable across multiple axes, aligning with specific test requirements.

The IDS UI-1540LE-M-GL camera is operated using the uEye Cockpit software program provided by IDS. The ideal settings for the experiment were established through testing and calibration. The optimal parameters include a pixel clock set at 5 MHz, a frame rate of 2.91 fps, and an exposure time of 5.126 ms. These settings ensure the highest quality image capture for the specific requirements of the experiment.

Environmental factors, including temperature fluctuations, airborne dust, and other disturbances, necessitate system alignment before each use. Additionally, mirrors require regular realignment after extended periods to account for atmospheric alterations.

A. CALIBRATION

Startup begins by activating the monochromatic laser source, PI and Thorlabs Piezo controllers, laser metrology system, and the imaging camera. The laser metrology system needs a period for thermal stability to stabilize the tracker. Because of the system's sensitivity to nanometer changes and the mirrors' micron-level movement, this stabilization is essential before any testing or data collection. Respective MATLAB codes and the PI software are initiated to bias the collector mirrors and compensating mirrors. Using the PI software, the compensating array tip/tilts and pistons are set to mid-range with values of 50 nm. The collector array ThorLab stages are adjusted to a mid-range of 35 V, either using the front panel controls or MATLAB software, ensuring the maximum range of motion for the piezo controllers to simulate and correct aberrations. With the laser source, the collector array mirror mounts are adjusted to make their spots approximately overlap in the far-field, as observed on the far-field camera. This laser source facilitates coarse adjustments. Panchromatic light is then initialized, and the spots in the far-field camera are overlapped using the Thorlabs piezo manual adjustments. The piston (z-axis) on the mounts of the three Thorlabs stages for the Collector Array mirrors is then fine-tuned. This adjustment continues until the overlapped airy disks produce white-light fringes, resulting in a pattern that resembles a “flower,” as depicted in Figure 31.

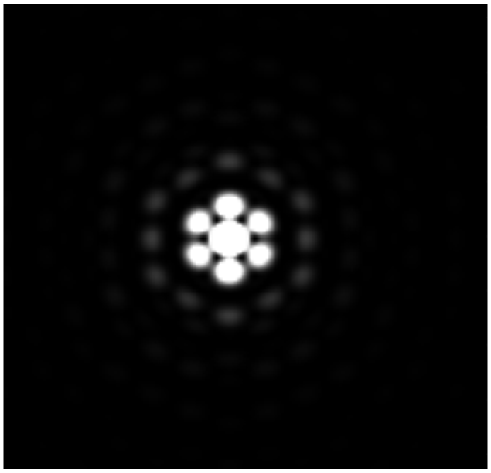

Figure 31. Ideal aligned 3-mirror collectors from computer simulation: flower pattern.

The “flower” or “flower petal” interference pattern indicates the relative alignment of the array mirrors in the optical setup. This pattern arises from the interference of overlapping light waves and shows the coherent overlap of multiple beams. It confirms that the optical components, especially the array mirrors, are positioned for beams from different paths to coherently intersect in the far-field [14]. The pattern’s sensitivity to alignment changes offers immediate feedback, ensuring quick detection of any misalignment or phase variance. The focus is not just on achieving this “flower” pattern but also on testing the combiner’s ability to maintain the aligned image when external disturbances are introduced. This method offers a thorough assessment of the system’s resilience and adaptability. The panchromatic point source light can be swapped with the

USAF Test image for further testing and evaluation. After aligning the mirrors, perturbations are introduced to test the compensator's correction capabilities.

(1) Testing Methods

To evaluate the combiner satellite's capability to stabilize the image, two tests were developed to introduce roll, yaw, and piston motion into the system. These motions correspond to the tip/tilt/piston movements in each mirror. MATLAB facilitated the control of the 6-DOF simulators, and the introduced motions simulate disturbances that a satellite formation might face during data collection. In this calibrated system, the satellite motions are directly linked to voltage inputs. A voltage range of ±37.5 V corresponds to a physical motion range of ±50 µm. This configuration means that when the system's actuators or motors receive a voltage input, they induce a motion proportional to that input. The maximum motion attainable is 50 µm in either direction when the peak voltage of 37.5 V is applied, ensuring precise adjustments and control over the roll, yaw, and piston motions.

b. Random Disturbances

The initial disturbance introduced was a series of random perturbations. This test was designed to emulate the unpredictable roll, yaw, and piston motions that each collector mirror might experience in a dynamic space environment, thereby assessing the system's resilience to unforeseen disturbances.

c. NASA JPL Disturbances

The second disturbance applied were the position control error from the NASA JPL study. As can be seen in Figure 14, the position control error for a Leader/Follower simulation was estimated to be less than 200 nm. To introduce an error corresponding to 200 nm in a system where ±37.5 V equate to ±50,000 nm, a conversion factor is first established. This factor is determined by dividing 50,000 nm by 37.5 V, resulting in approximately 1,333.33 nm/V. Using this conversion, an error of 200 nm translates to about 0.15 V. The nature of the error application can vary so a random value generator to produce values between -0.15 and +0.15 V was applied to the system.

B. SIMULATION MODEL AND SIMULATION SETUP

A Leader/Follower model was created in MATLAB to assess the performance of the sparse aperture system under realistic satellite formation flying conditions. The test aimed to validate the robustness and reliability of the sparse aperture system in real-world scenarios by replicating the intricate dynamics of satellite motion in formation. In this MATLAB simulation, a Leader/Follower satellite formation architecture is modeled, leveraging the Aerospace Blockset. The simulation is an extension of MATLAB's prebuilt example, "Modeling Custom Satellite Attitude and Gimbal Steering" [25]. The model simulates the dynamics of a Leader/Follower satellite formation, all equipped with conical imaging sensors. The formation is tasked with executing a targeted flyover mission over specific regions on Earth, such as Ukraine and Taiwan for this study.

The leader satellite serves as the primary spacecraft within the formation. Its attitude and position are precomputed based on the target region and loaded into the model. These computations are derived from the Sparse Aperture Trajectory Simulation (refer to Figure 32), which generates the requisite quaternion profile for the satellite to fly over the target, whether in a nadir-pointing or geographic-pointing configuration.

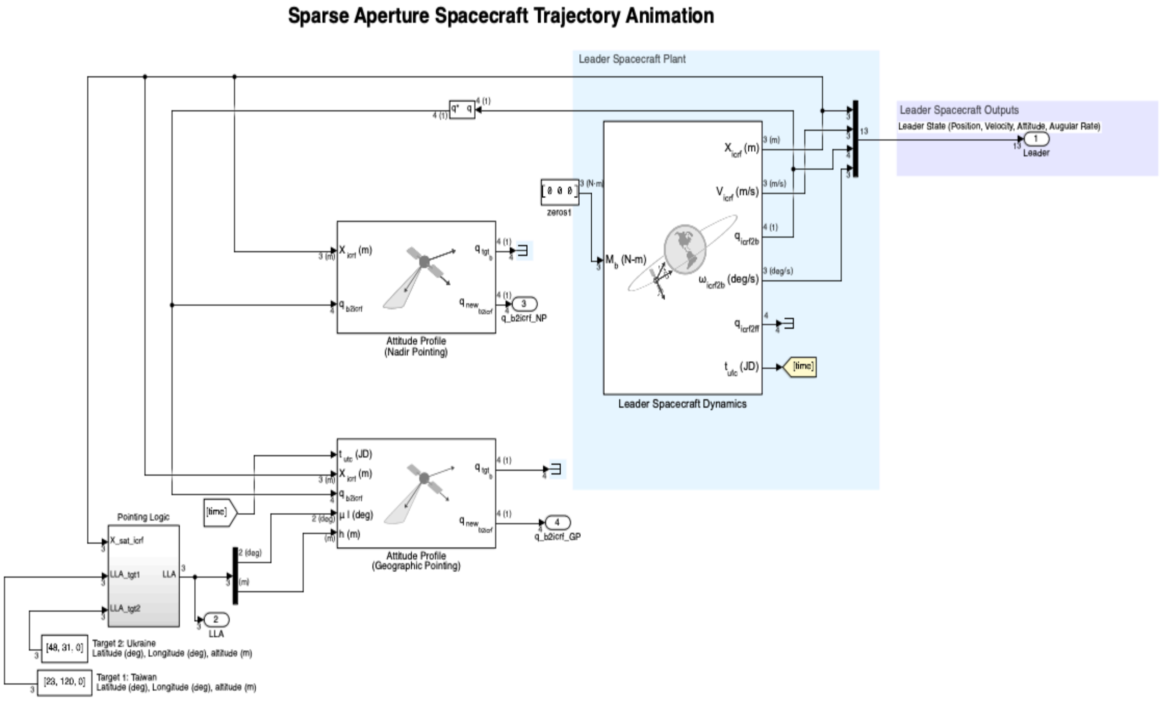

Figure 32. Sparse aperture trajectory simulation.

The follower satellites are strategically positioned in a triangular formation relative to the leader. This geometry is achieved by defining their relative positions in the leader's body frame, which are then transformed into the inertial frame using the leader's attitude quaternion. In Figure 33, the followers—labeled F1, F2, and F3—are positioned 200,000 m away from the leader (labeled L), forming an equilateral triangle. This specific distance is chosen because it allows the individual satellites to be discernible in the visualization; any closer, and they would not be distinguishable. However, 3 m between followers and 60 m from the leader would be used in realistic simulation. These distances are selected to reflect a more practical formation geometry that could be implemented in real-world satellite constellations.

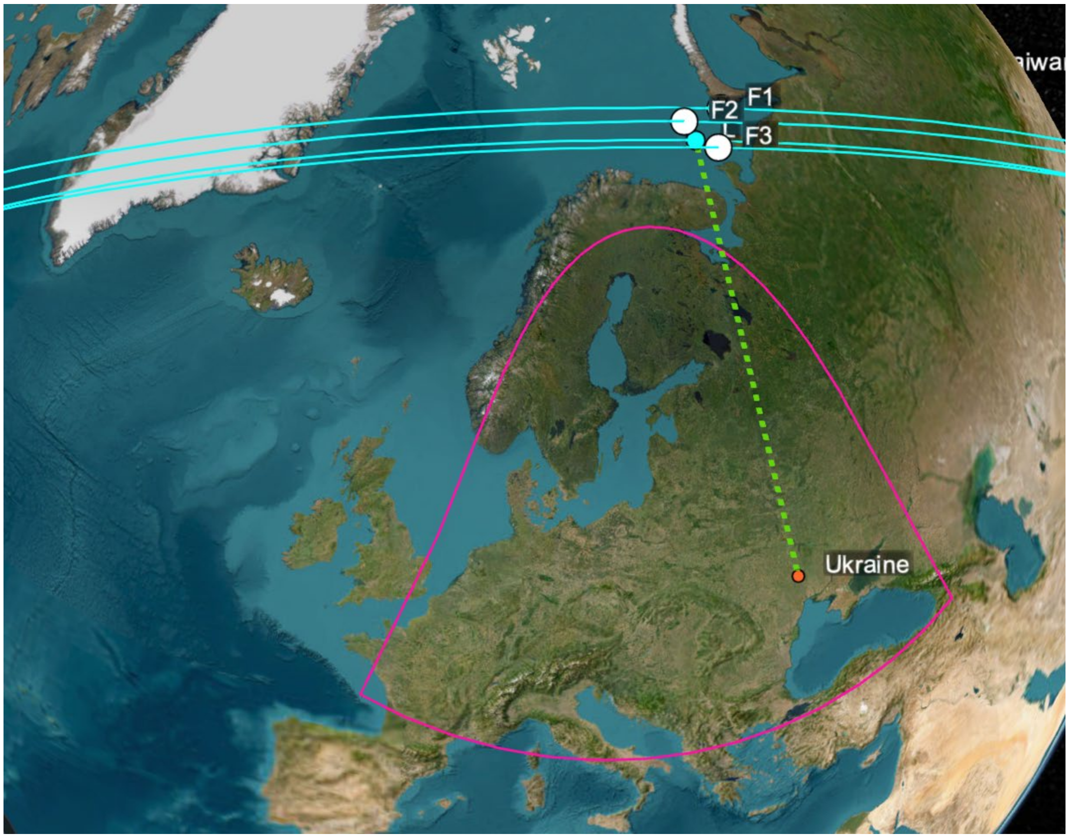

Figure 33. L/F formation flyover of Ukraine.

The simulation model is predicated on the assumption that the follower satellites will maintain a triangular formation relative to the leader satellite for the entire duration of the mission. This formation is programmed to operate in MEO over a period of 5400 s (90 min), with specific orbital parameters detailed in Table 1. As the satellites progress along their orbital path, they maintain a nadir-pointing orientation until they approach the vicinity of their designated target. At this point, the satellites adjust their orientation to facilitate image capture. Concurrently, the model computes the attitude error between the leader and follower satellites. Future work aims to translate this error data into conditions applicable to the sparse aperture test table. This will provide valuable insights into potential adjustments needed to enhance the imaging capabilities of the satellite formation.

Table 1. Sparse aperture simulation orbital elements.

Orbital Element	**Values**
Semi-major axis	7260 km
Eccentricity	0.05
Inclination	70°
Argument of Periapsis	0°
Right Ascension of the Ascending Node	215°
True Anomaly	200°

C. OBSERVED METRICS

A systematic methodology employing eight pivotal metrics has been established to assess the performance and adaptability of the sparse aperture system. Each metric will be presented in the context of three distinct image states: the initial "perfect" image, the image without corrections, and the image post-correction. The metric will be focused on the results from the panchromatic light source for this study. This approach aims to provide a thorough evaluation of the system's ability to rectify disturbances and uphold optimal imaging quality.

1. Applied Disturbances:

This metric measures the error applied to each mirror, with a focus on roll, yaw, and piston motions.

2. Interferometric Measurements:

This captures the deviation of each collector mirror from its baseline due to the introduced disturbances.

3. Applied Corrections:

This details the adjustments made to each combiner mirror to counterbalance the disturbances.

4. Image Before and After:

This section offers a direct comparison of images before disturbances and after corrections, highlighting any potential degradation in image quality and the system's corrective capability.

5. PSF:

Representation: The PSF characterizes the system's reaction to a point source, acting as an indicator of imaging quality and resolution.

Direct Comparison: By comparing the PSF before disturbances and after corrections, the system's resilience becomes evident, revealing both potential image sharpness degradation and the system's capability in addressing such issues.

6. SNR (Signal-to-Noise Ratio):

SNR evaluates the ratio of signal power to noise power in an image. In the context of PSF, a high SNR ensures the clarity of the main lobe, essential for accurate imaging [26].

7. RMSE (Root Mean Square Error):

RMSE measures the difference between predicted and observed values. For PSF, it assesses how much the disturbed PSF deviates from an ideal state. A lower RMSE indicates effective disturbance correction [27].

8. FWHM:

FWHM gauges the width of the PSF's main lobe at half its peak value, providing insights into the system's resolution. Monitoring FWHM changes post disturbances can indicate the system's ability to maintain or recover its resolution [5].

A detailed analysis of these metrics provides insight into the sparse aperture system's ability to correct disturbances. This approach offers both quantitative and qualitative assessments of the system's resilience and adaptability.

THIS PAGE INTENTIONALLY LEFT BLANK

V. ANALYSIS

A comprehensive simulation and experimental analysis evaluated the sparse aperture system's adaptability and performance using both a panchromatic white light and an USAF test image. This chapter showcases results from two distinct disturbance scenarios: Random Disturbances and disturbances derived from the NASA JPL study. The disturbance scenarios will last for a time of 120 s. The examination details the applied disturbances, corrective measures, and associated laser interferometric measurements. Uncorrected images highlight the system's response without corrective actions, setting a benchmark for evaluating correction efficacy. The analysis compares the "Initial" outcomes with the "Uncorrected" and "Corrected" results. A PSF comparison remains central, serving as a key metric to assess the system's imaging quality maintenance or restoration across disturbance scenarios.

A. RANDOM DISTURBANCES (RD)

1. Applied Disturbances

As shown in Figure 34, disturbances are introduced in the roll, yaw, and piston motions of each mirror for a timespan of 120 s. These disturbances, generated using an algorithm in MATLAB, mimic the unpredictable challenges that individual satellites in a formation might face. These challenges can be due to factors such as environmental conditions, mechanical issues, or other external interferences. The intention is to replicate real-world scenarios and evaluate the system's ability to adapt and respond effectively.

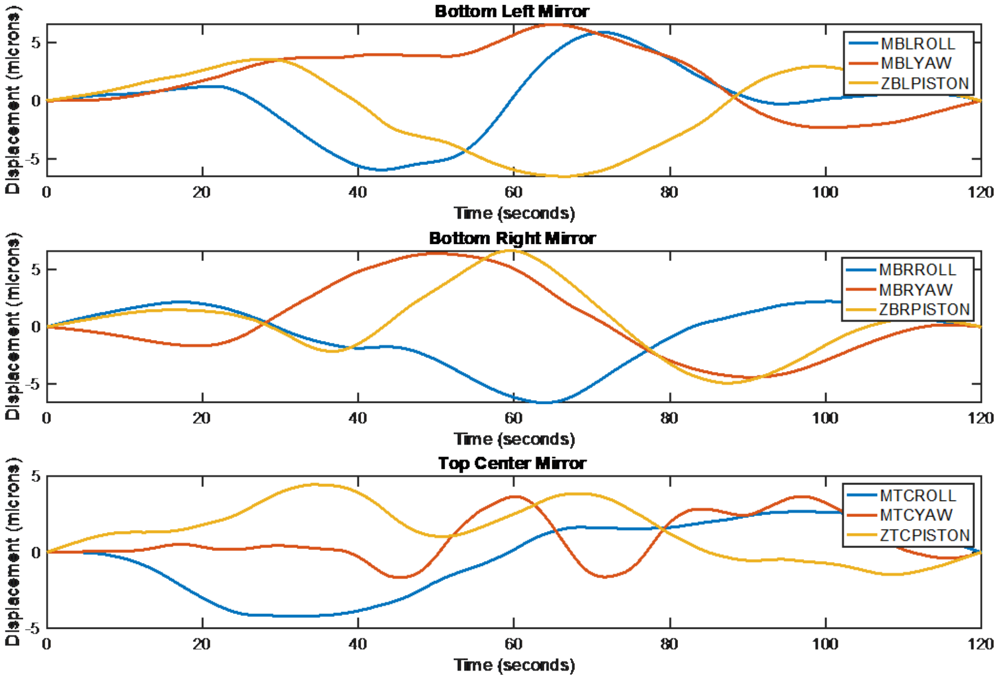

Figure 34. RD: Applied disturbances to collector mirrors.

2. Interferometric Measurements

As presented in Figure 35, the laser measurement system tracks the positional shifts of each mirror, using its initial central position as the baseline reference. Each distinct line plotted signifies a unique corner cube, effectively serving as a visual testament to the mirror's response to external perturbations.

In the initial phase, notably up to the 10 s mark, both graphs mirror each other's stability. Figure 34 reveals minimal to no disturbances, and this little change is mirrored in Figure 35, which showcases negligible displacement from the mirrors' center point.

After the 10 s mark, as disturbances become more pronounced, the laser measurements show how the mirrors move in response, capturing the mirrors' deviations. This phase illustrates the system's real-time response to external challenges.

Overall, the close match between the disturbances and the laser measurements gives a good idea of how well the system can handle changes and fix any issues. It offers invaluable insights into the system's inherent resilience, adaptability, and the effectiveness of any corrective mechanisms in place.

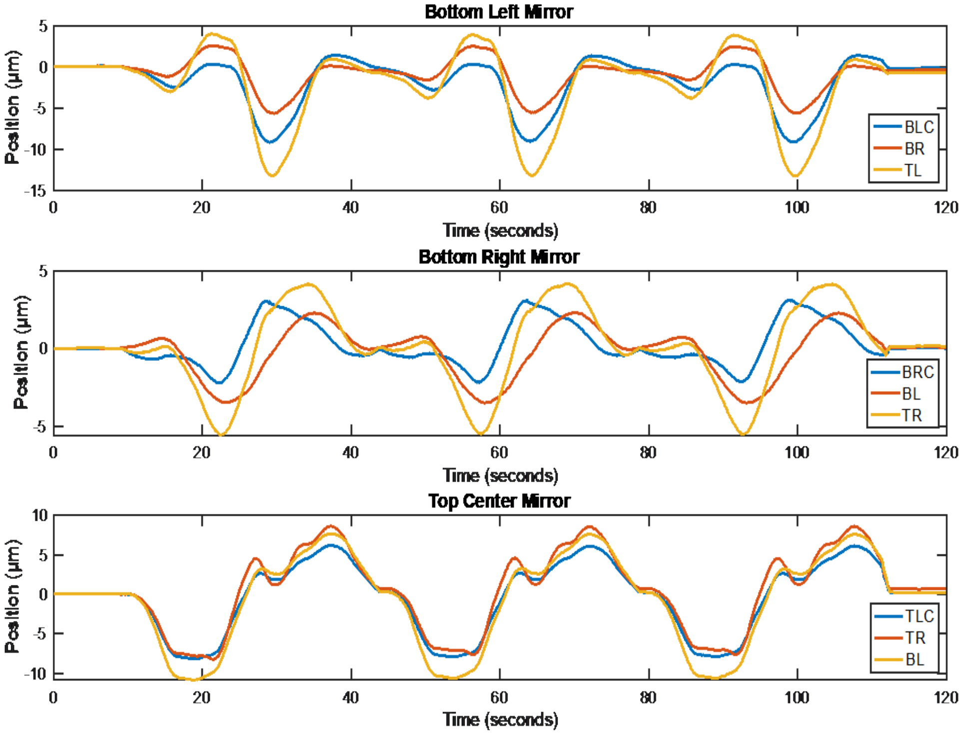

Figure 35. RD: Laser interferometer measurements.

3. Applied Corrections

The laser interferometric system serves as a critical instrument in monitoring disturbances within the sparse aperture setup. Using data from this system, a transformation matrix is created that translates observed disturbances into actionable corrections for the combiner mirrors.

The system, however, exhibits a lagging characteristic. This means that there is an inherent delay between when a disturbance is detected and when the system responds with corrective measures. This time lag becomes evident when comparing the trends in Figure

34 with the corresponding actions in the Figures 36 and 37. It encompasses the duration taken to measure, interpret, and execute the necessary adjustments.

To address the disturbances, the system employs corrections primarily in the form of tip and tilt motions, measured in microradians, and piston motions, measured in microns. This can be viewed in Figures 36 and 37. These specific adjustments aim to counteract the disturbances and realign the mirrors, ensuring optimal performance despite external challenges.

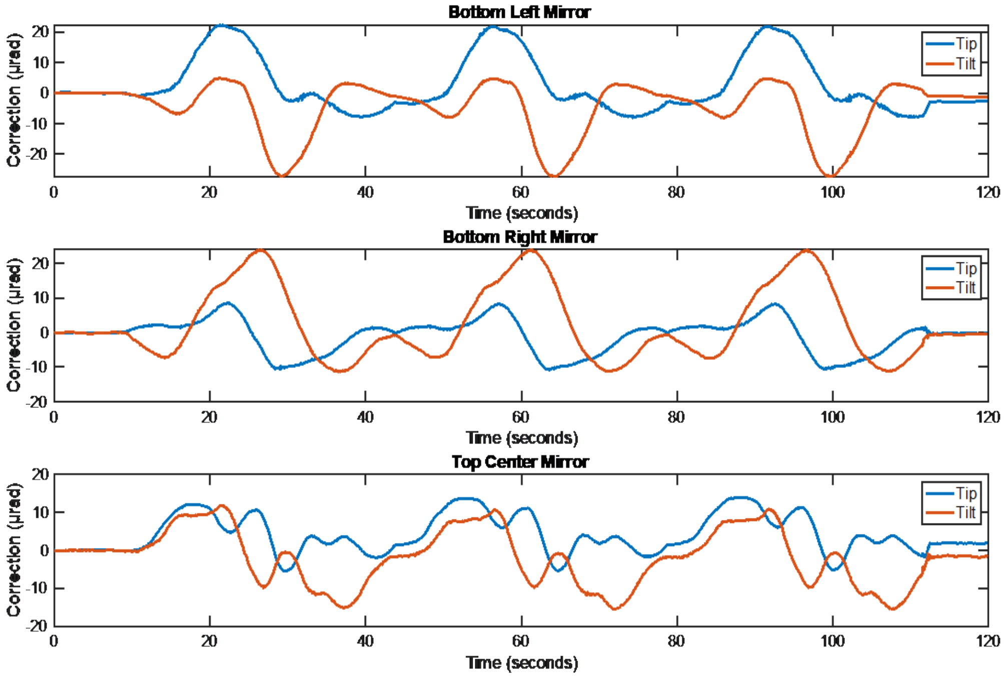

Figure 36. RD: Tip/tilt corrections to combiner mirrors.

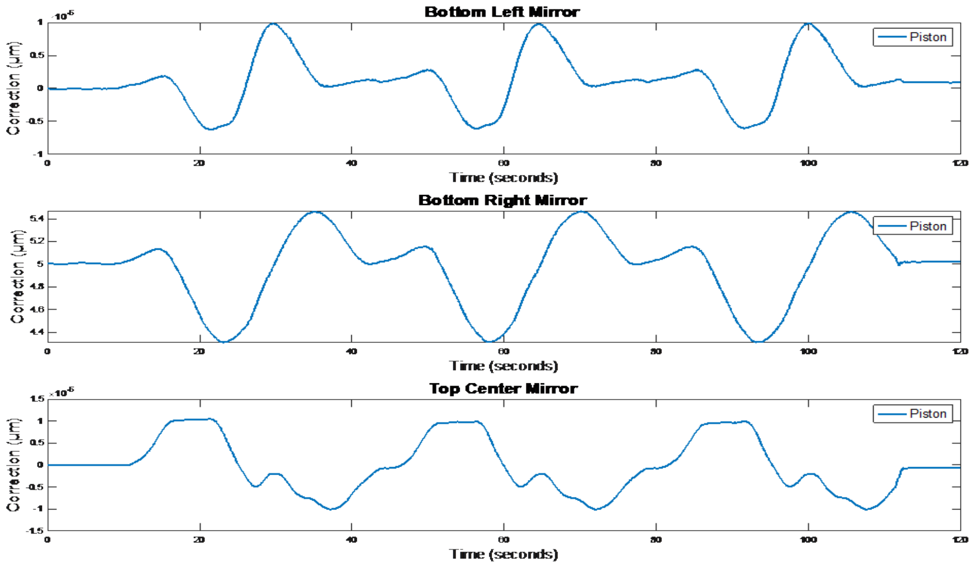
Bottom Left Mirror

Bottom Right Mirror

Top Center Mirror

Figure 37. RD: Piston corrections to combiner mirrors.

4. Images

Figure 38 includes a perfect reference image of both panchromatic light and the USAF test image for comparison. The sparse aperture system starts with the collector mirrors aligned to produce a clear initial image, seen in Figure 38. This alignment ensures optimal imaging, capturing details with precision. As the system operates, disturbances are applied, seen in Figure 34, compromising the image's clarity and fidelity.

To counteract these disturbances, the system uses combiner mirrors as a corrective mechanism. These mirrors adjust to correct errors and aim to restore the image quality. The corrected images in Figure 38 show the result of this intervention at a timestamp of 100 s, highlighting the system's ability to maintain image integrity.

For a comprehensive understanding, it is essential to see the system's output without any corrections. The uncorrected images of the panchromatic light and AF test image show image degradation due to the lack of compensations. Notably, three distinct lights or AF test images spread out because the combiner mirrors are not merging the images. This dispersion underscores the importance of the combiner mirrors in the system's overall performance.

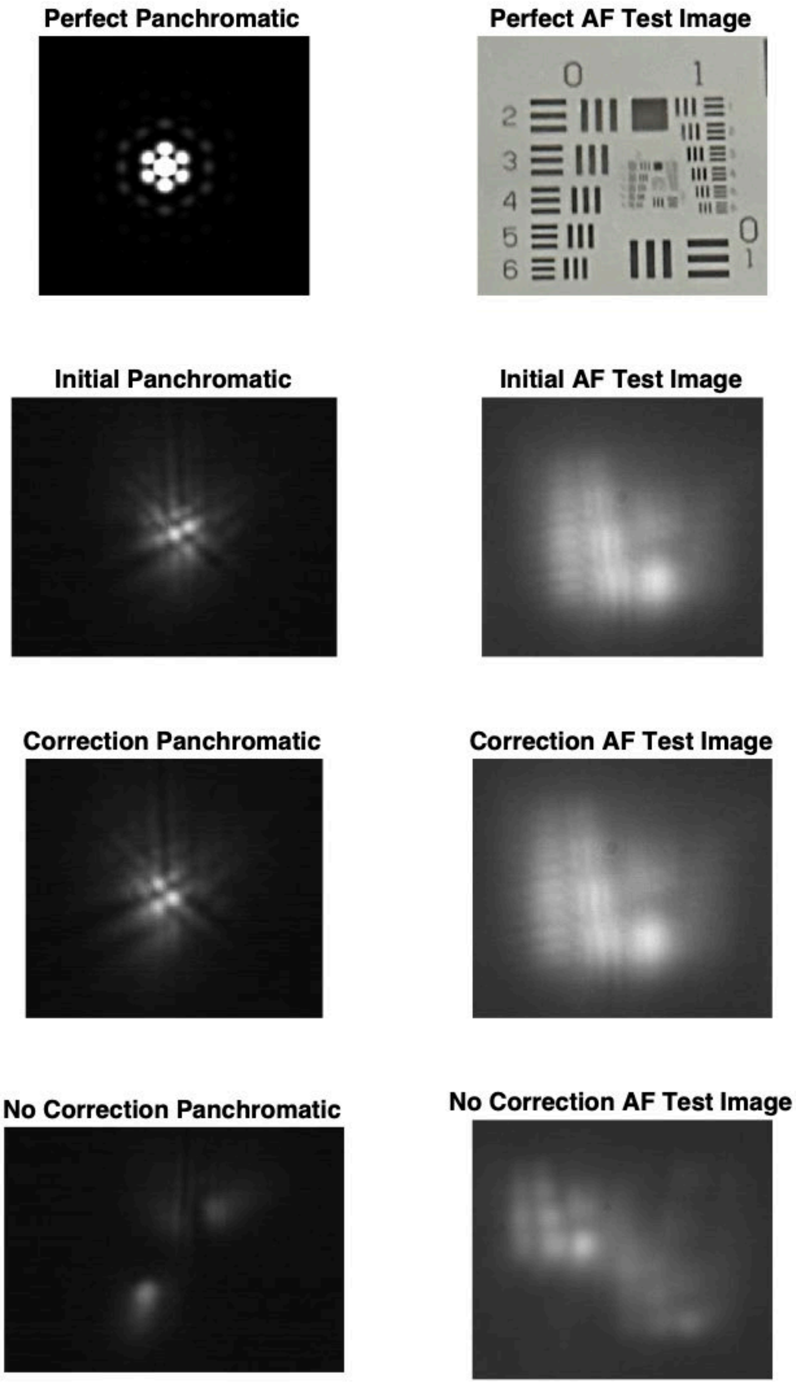

Figure 38. RD: Panchromatic and USAF test images.

5. PSF Comparison

The initial PSF, with an intensity of 0.92, showcases sharp and focused features centered on the graph, a clear sign of optimally aligned mirrors. This can be seen in Figure 39. This clarity sets the benchmark for the system's peak performance. In contrast, the corrected image, with an intensity of 0.90, demonstrates the system's ability to counter disturbances and realign the image. The precision and central focus of this PSF, seen in Figure 40, closely mirror that of the initial PSF, indicating successful compensation. On the other hand, the uncorrected image seen in Figure 41, with a significantly reduced intensity of 0.45, underscores the system's challenges when disturbances go unchecked. This image presents three distinct peaks with varying intensities, signifying a degraded or defocused state compared to the initial PSF.

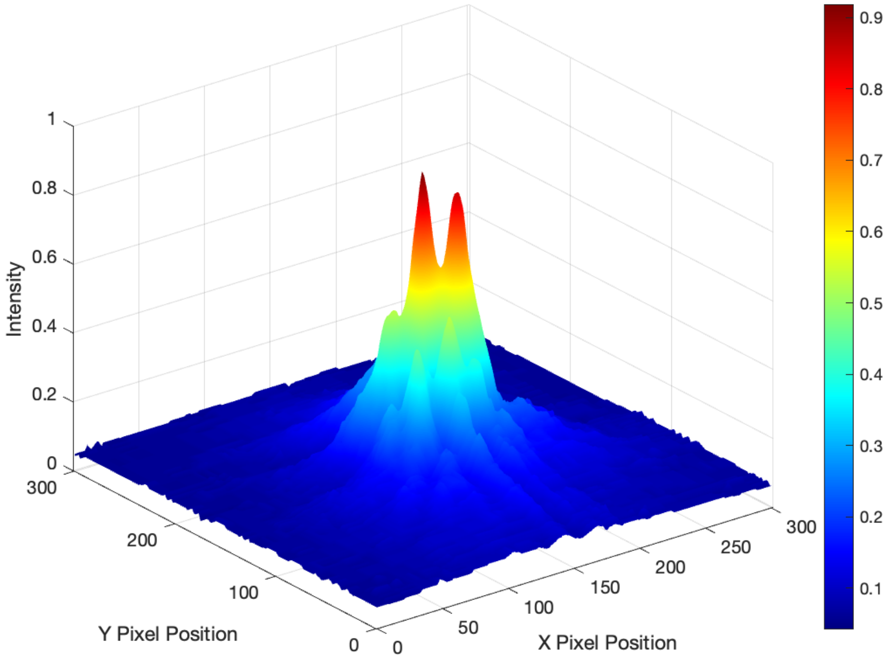

Figure 39. RD: Initial PSF for panchromatic light.

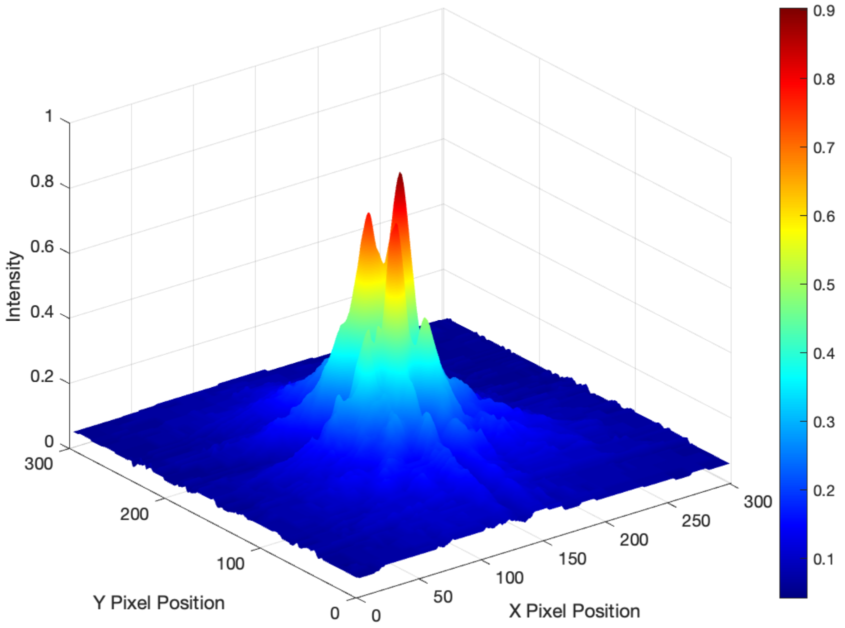

Figure 40. RD: Corrected PSF for panchromatic light.

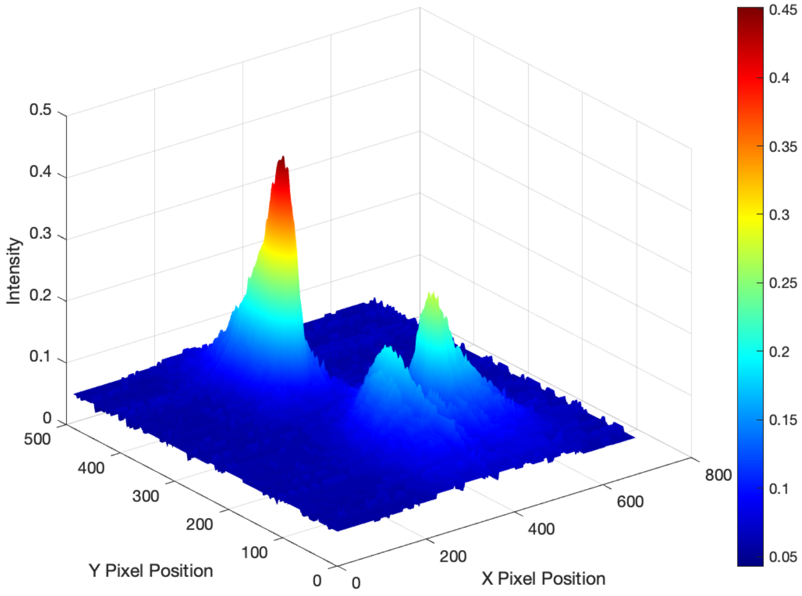

Figure 41. RD: Uncorrected PSF for panchromatic light.

Metrics in Table 2 offer a comparison of image qualities by calculating the PSNR, RMSE, and FWHM values. The initial image serves as the standard in this comparison. Metrics like RMSE and PSNR provide insight into the differences or errors between two images. In the context of this analysis, the initial image serves as a reference so comparing the initial image to itself using RMSE will always yield a value of zero, indicating no difference, and consequently, the PSNR will be infinite. RMSE and PSNR values will be omitted for the initial image. The FWHM for the initial image has values of 35 px horizontally and 41 px vertically. These values represent the inherent spread or blur in the initial image and will provide a baseline against which the other images will be compared.

The uncorrected image, when compared to the initial image, exhibits notable discrepancies. Its RMSE stands at 0.11. This high RMSE indicates that there are significant differences in pixel values between the uncorrected and initial images. The PSNR for this image is 19.7 dB, the lowest among the images. A lower PSNR value suggests a greater difference in quality between the uncorrected and initial images. The uncorrected image's FWHM values are 50 px horizontally and 70 px vertically. These are the largest FWHM values among the three images, suggesting that the uncorrected image has the most spread or blur.

The corrected image shows improvement over the uncorrected image, especially when compared to the initial image. The RMSE for the corrected image is 0.05, significantly lower than that of the uncorrected image. This indicates that the correction process has effectively brought the image closer to the initial image in terms of pixel values. The PSNR of the corrected image is 25.6 dB, indicating a better quality than the uncorrected image when benchmarked against the initial image. This improvement in PSNR suggests that the correction process has indeed enhanced the image's quality. The FWHM values for the corrected image are 30 px horizontally and 41 px vertically, smaller than that of the uncorrected image. The similar FWHM values implies that the correction process has effectively reduced the image's blur, rendering it sharper.

Table 2. Random disturbance panchromatic light metrics.

Image	**Highest Intensity (pixels)**	**PSNR (dB)**	**RMSE**	**FWHM-Horizontal (pixels)**	**FWHM-Vertical (pixels)**
Initial Image	0.92	N/A	N/A	35.0	41.0
Corrected Image	0.90	25.66	0.05	30.0	41.0
Uncorrected Image	0.45	19.71	0.11	50.0	70.0

B. NASA DISTURBANCES

1. Applied Disturbances

The second disturbance applied was sourced from the NASA JPL study, specifically pertaining to position control errors. This study, focusing on a Leader/Follower satellite simulation, estimated the position control error to be less than 200 nm. Figure 42 illustrates the application of this error. Given the dynamic nature of satellite formations and their susceptibility to varying disturbances, a random value generator was employed in MATLAB. This generator produced values ranging between -0.15 and +0.15 V derived from translating nanometers to an equivalent voltage, ensuring a realistic representation of the position control error's impact on the system. The fluctuations and trends observed in the graph offer insights into how such an error, though seemingly minuscule, can influence the system's behavior and performance.

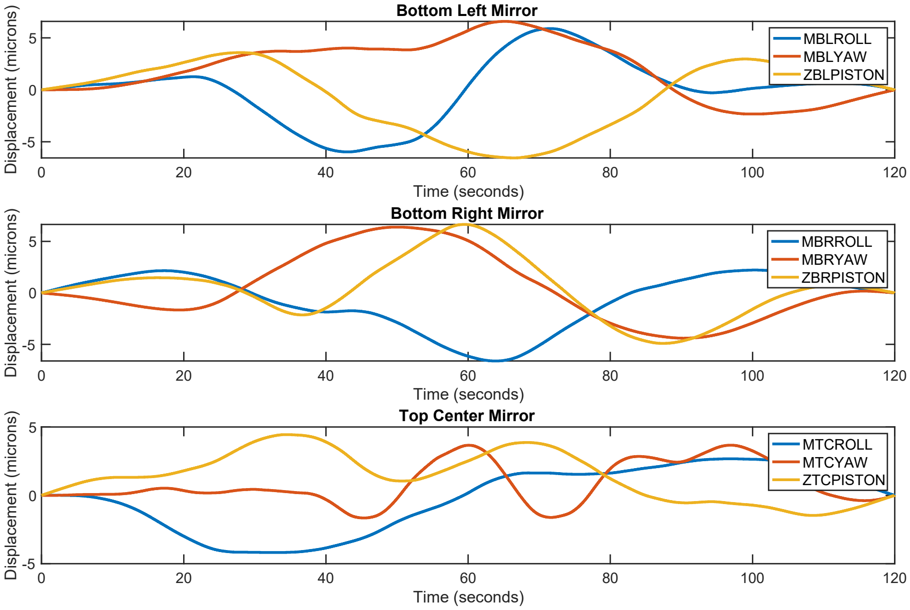

Figure 42. NASA: Applied disturbances to combiner mirrors.

2. Interferometric Measurements

Figures 42 and 43 both start with a stable phase. This undisturbed phase in Figure 42 matches the steady state in Figure 43. When disturbances are introduced, significant fluctuations appear in Figure 43, mirroring the disturbances shown in Figure 42 The magnitude of these fluctuations in the measurements matches the severity of the disturbances, indicating the system’s reactions are in proportion to the introduced challenges. There may be a slight lag between the start of a disturbance and the system’s response, reflecting the system’s inherent reaction time. Continuous variations in the measurements, even between new disturbance introductions, highlight the system’s sensitivity and its ability to detect ongoing disturbances. Overall, the system seems both alert and consistent, modifying its behavior based on the disturbances it faces, with subsequent corrections handled by the combiner mirrors.

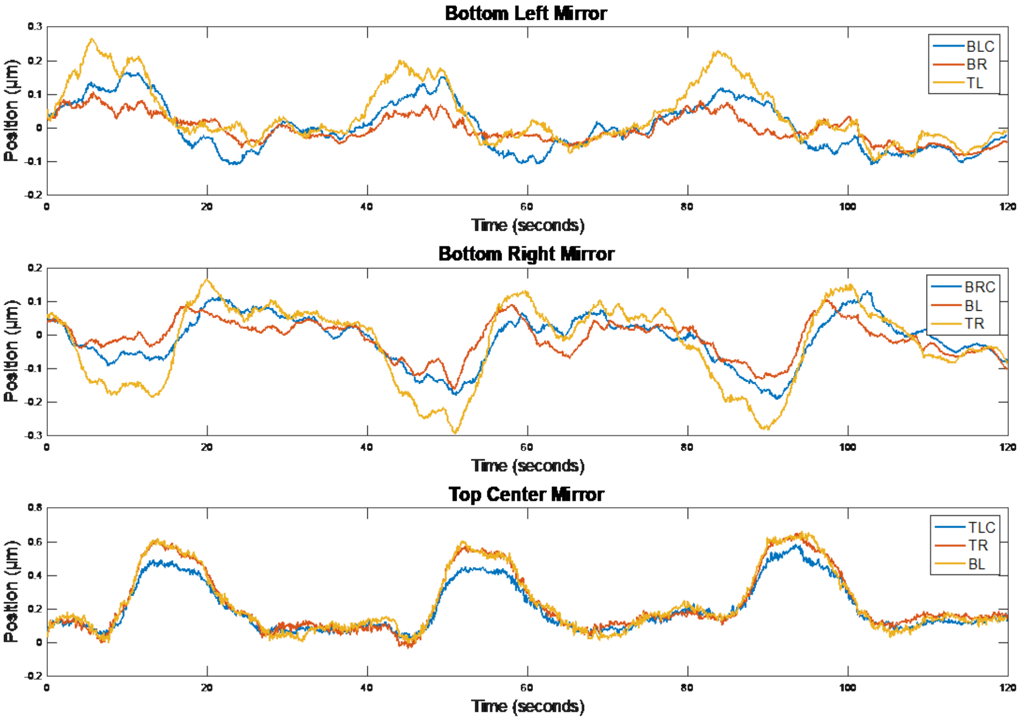

Figure 43. NASA: Laser interferometer measurements.

3. Applied Corrections

Figures 44 and 45 illustrate the compensatory actions employed by the combiner mirrors in response to the disturbances introduced to the system. Each line in the graph represents the correction applied to individual mirrors. The variations in the graph, corresponding to the time and magnitude of the disturbances from Figure 42, demonstrate the system's active effort to restore its optimal state. The applied corrections taken by the combiner mirrors represent how the system dynamically adjusts, employing the combiner mirrors as a corrective mechanism to counteract disturbances. It is evident that the system not only detects disturbances but also actively works to mitigate their impact, ensuring the preservation of image integrity.

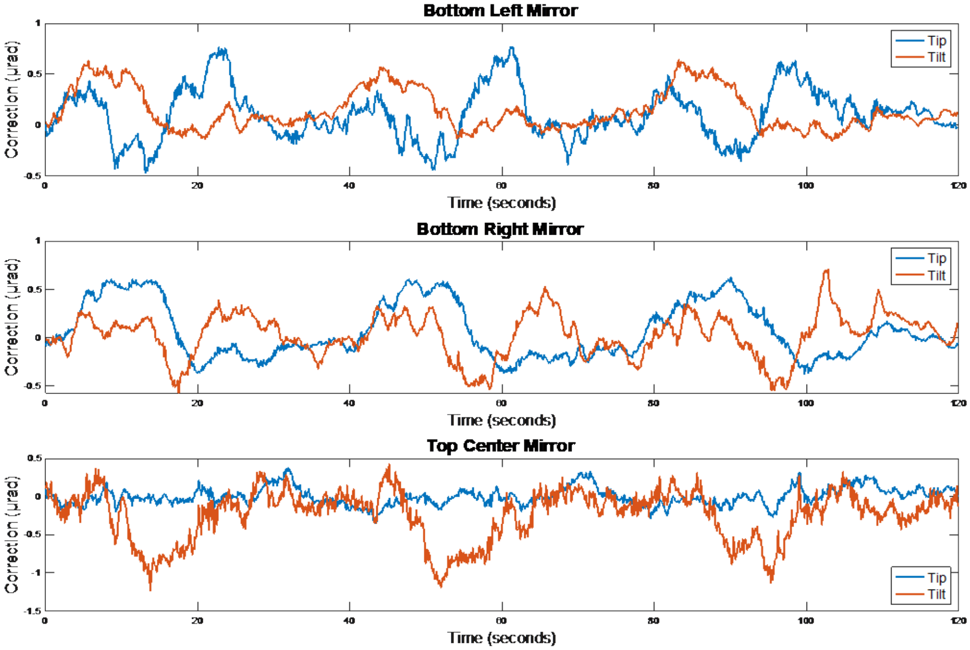

Figure 44. NASA: Tip/tilt corrections to combiner mirrors.

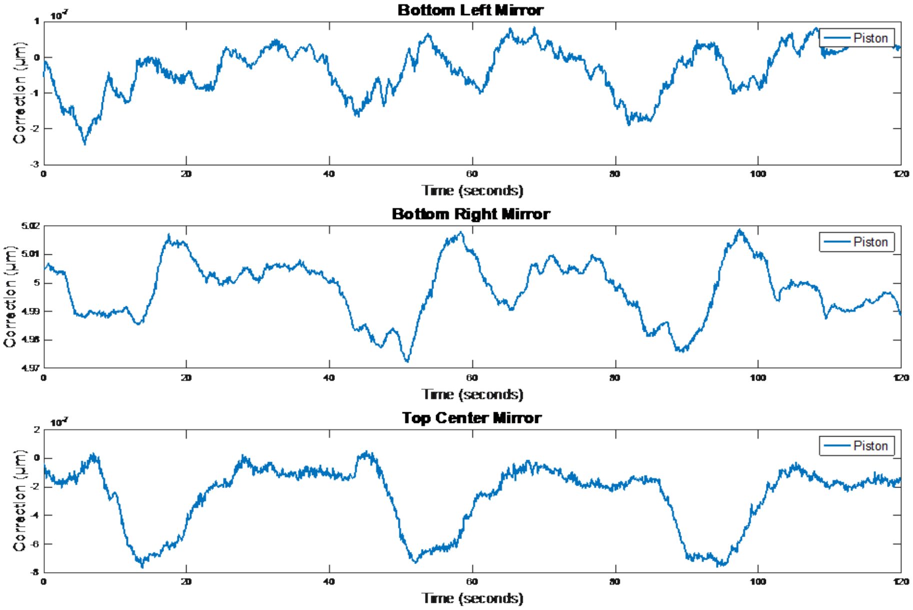

Figure 45. NASA: Piston corrections to combiner mirrors.

4. Images

The sparse aperture system begins with collector mirrors in optimal alignment, as depicted in Figure 46, producing a clear initial image. Disturbances during operation can compromise the image’s clarity. Combiner mirrors intervene to address these challenges. Their corrective actions strive to restore or maintain the image’s original quality, as seen in the corrected images in Figure 46, taken at a timestamp of 100 s. The Correction Panchromatic and Correction AF Test Image look similar to the initial images with both intensity and resolution. Observing the system without these corrections offers insights. Image divergence becomes evident in the degraded no-correction panchromatic and AF test image in Figure 46. The intensity and spread of the image highlight the combiner mirrors critical role in ensuring consistent imaging quality.

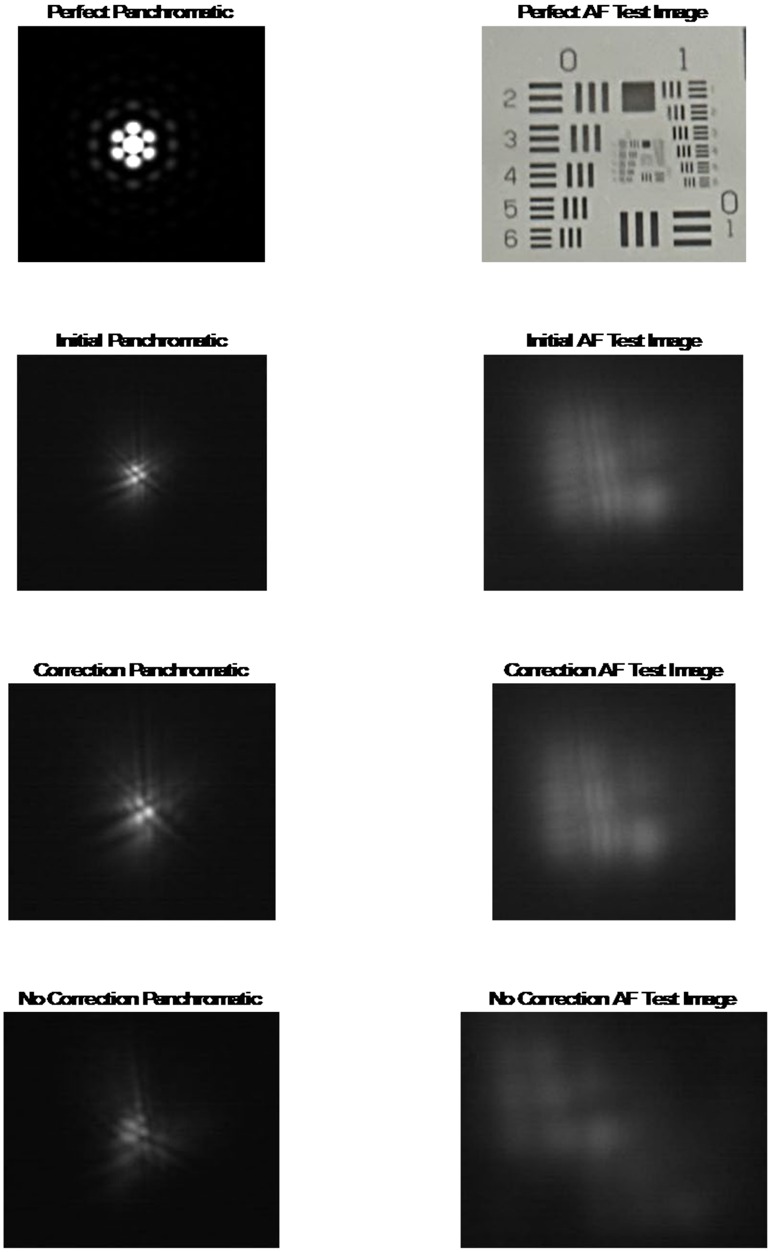

Figure 46. NASA: Panchromatic and USAF test images.

5. PSF Comparison

Similar to the Random Disturbance study, the initial PSF depicted in Figure 47 exhibits characteristics of an optimally aligned mirror system. The graph's center is marked by sharp, focused features with a high intensity of 0.91, serving as a benchmark for the system's peak performance. Figure 48 presents the corrected image, mirroring the initial PSF's sharpness and central focus, with a slightly reduced intensity of 0.89. This similarity indicates effective compensation for disturbances.

However, the uncorrected image shown in Figure 49 greatly deviates from the initial and corrected images. It is characterized by multiple peaks with significantly weaker and more varied intensities, peaking at only 0.47. This dispersion and reduction in intensity signal a degraded or defocused state, underscoring the detrimental impact of unaddressed disturbances on the system's imaging capabilities.

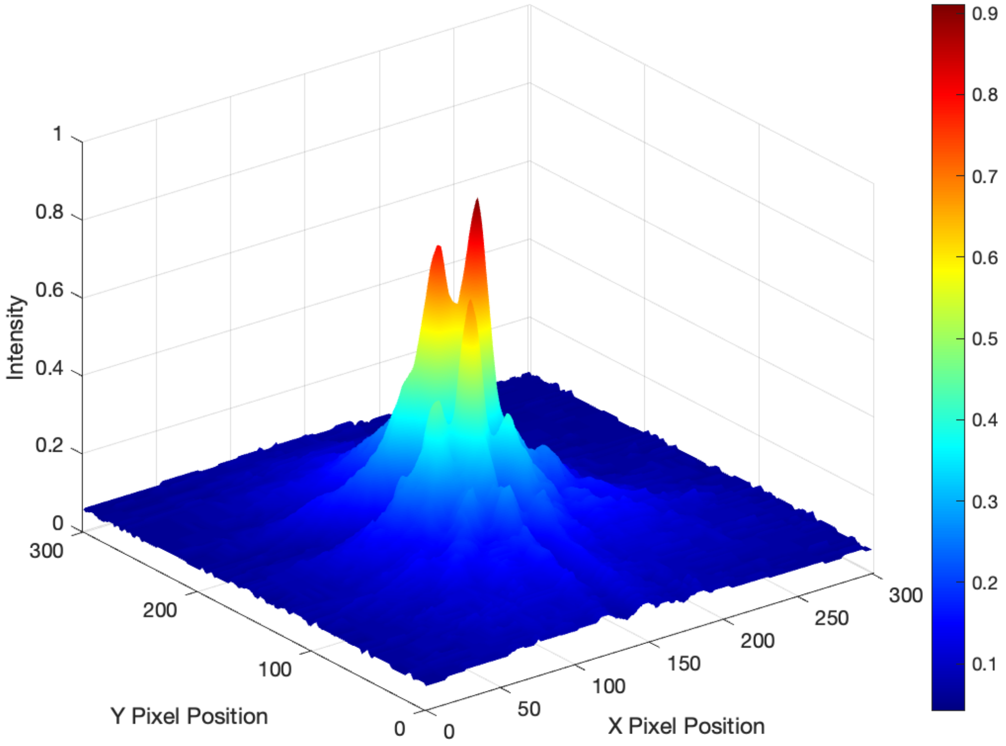

Figure 47. NASA: Initial PSF for panchromatic light.

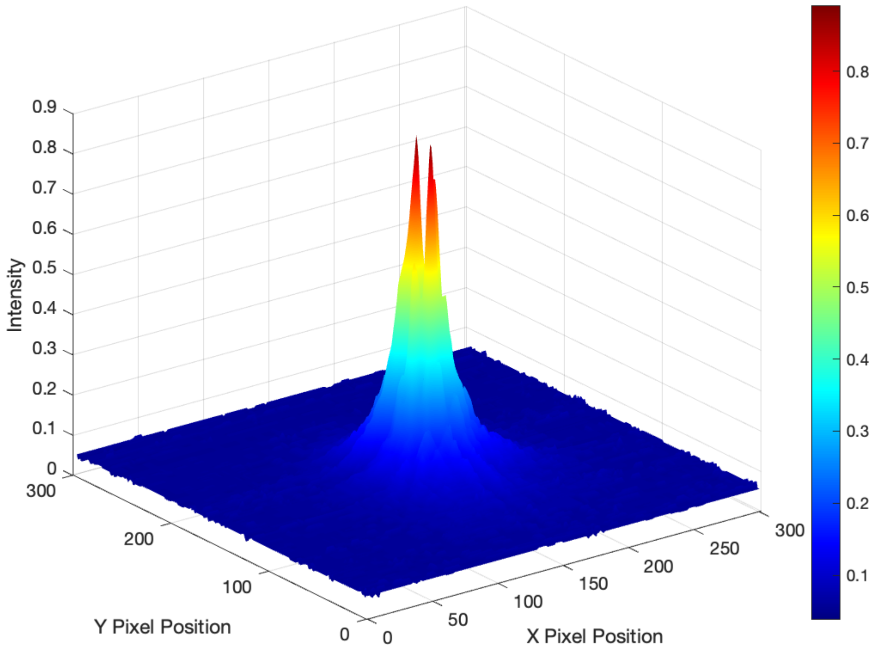

Figure 48. NASA: Corrected PSF for panchromatic light.

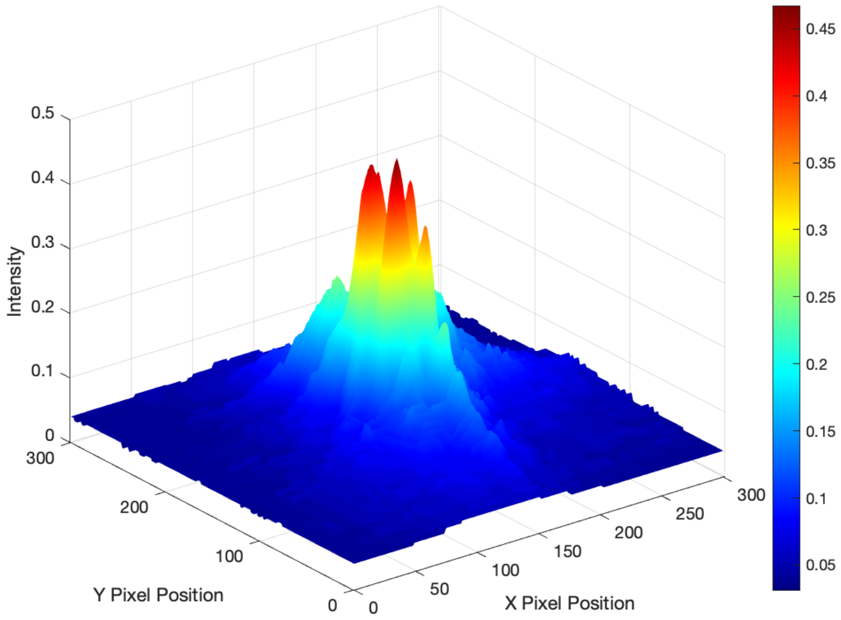

Figure 49. NASA: Uncorrected PSF for panchromatic light.

The metrics for the image quality were calculated and are presented in Table 3. The initial image serves as the standard for comparison. The PSNR and RMSE values are omitted as previously discussed. The FWHM measures 13.0 px horizontally and 25.0 px vertically, setting a baseline for other images by representing the inherent spread in the initial image.

Clear differences emerge when comparing the uncorrected image to the initial image. It registers an RMSE of 0.11, signaling notable pixel value discrepancies. Its PSNR stands at 18.81 dB, lower than the initial image's, implying reduced image quality. FWHM values for the uncorrected image are 34.0 px horizontally and 47.0 px vertically, showing more spread or blur.

The corrected image shows improvements over the uncorrected image when compared to the initial image. Its RMSE drops to 0.08, indicating that the correction process has made the image more similar to the initial image. The PSNR for the corrected image is 22.24 dB, suggesting enhanced image quality compared to the uncorrected image. FWHM measurements for the corrected image are 27.0 px horizontally and 23.0 px vertically, both closer to the initial image's values. This suggests that the correction process has effectively reduced blur, enhancing image sharpness.

Table 3. NASA disturbances panchromatic light metrics.

Image	**Highest Intensity (pixels)**	**PSNR (dB)**	**RMSE**	**FWHM-Horizontal (pixels)**	**FWHM-Vertical (pixels)**
Initial Image	0.91	N/A	N/A	13.0	25.0
Corrected Image	0.89	22.24	0.08	27.0	23.0
Uncorrected Image	0.47	18.81	0.11	34.0	47.0

VI. CONCLUSIONS AND FUTURE WORK

This chapter outlines the principal findings of the thesis and considers avenues for further research.

A. CONCLUSIONS

In this thesis, the feasibility and effectiveness of a sparse aperture optical system through the development and implementation of a laboratory testbed were explored. The primary objective of this study was to determine whether a combiner satellite could effectively compensate for aberrations experienced by collector satellites. This was tested by subjecting the system to a variety of error types, including random errors and errors derived from a NASA JPL study.

The testbed was controlled by three software programs: MATLAB, PIMikroMove, and uEye Cockpit. This proved instrumental in introducing errors, measuring collector mirror displacements, and assessing the PSF of the images. The integration of the Zygo laser metrology system with its sub-nanometer resolution displacement measurement boards was pivotal in ensuring precise data acquisition and transfer.

The dual control mechanisms of the Thorlabs 6-DOF simulators, both manual and software-based, facilitated the simulation of satellite formation motion. The mapping and designation of each channel for computerized control, coupled with the development of diverse MATLAB scripts, enabled the simulation of user-specified motion trajectories.

Environmental factors were duly considered, necessitating system alignment before each use and regular realignment of mirrors to account for atmospheric changes. The testbed's design, incorporating a formation flying satellite platform, high-precision metrology, and an alignment and phasing system, was instrumental in providing real-time data on image collection and distortion for a simulated satellite formation concept.

The testbed's capability to simulate the motion of a sparse aperture using a laser metrology system and to correct aberrations through a combiner platform was a testament to its design and implementation. The coherent combination of light captured by the CCD imaging camera for analysis further validated the system’s efficacy.

This thesis has demonstrated the integrated sparse aperture system concept, laying a solid foundation for future research and development in this field. The combiner platform effectively corrected aberrations caused by applied disturbances, producing images comparable to the initial, undisturbed ones. Moreover, it displayed the significance of corrections by highlighting the degraded quality of images without them.

The testbed showcases the potential of sparse aperture systems to enhance the capabilities of satellite formations and their imaging applications. This testbed is not only a capable design but also a foundational step towards advanced studies and the potential integration of such systems into real-world satellite formations. This promises significant advancements in the fields of remote sensing and space exploration, opening new horizons for technological innovation and scientific discovery.

B. FUTURE WORK

The sparse aperture testbed has proven effective in applying and correcting formation flight errors. However, this work opens the door to numerous opportunities for future enhancements, setting a foundation for ongoing advancements in the field.

1. Wavefront Sensing and Metrology System

The current system operates on a closed-loop control framework, utilizing a laser interferometer system paired with a combiner platform to promptly correct misalignments. This setup is fundamentally dependent on a precise metrology system to ensure the combiner platform corrects any aberrations as the light comes into the combiner mirrors. However, the potential application of alternative wavefront sensing methods, especially those incorporating deep learning techniques, offers a promising direction for system enhancement.

In the current landscape where artificial intelligence is becoming increasingly prevalent, the application of deep learning for wavefront detection and correction could significantly improve both accuracy and operational efficiency. For the testbed, a feasible strategy involves constructing a detailed database of uncorrected images, each characterized by specific metrics. This database would act as a foundational dataset for training an AI model, such as a convolutional neural network, enabling it to identify and feed the needed corrections to the combiner platform.

This innovative approach could transform the existing system, potentially reducing or even eliminating the reliance on traditional metrology systems. Another method is that the collector mirrors could directly transmit images to the AI model, which, utilizing its trained database, could execute corrections autonomously. This advancement not only simplifies the correction process but also paves the way for more adaptive and robust sparse aperture systems in the future.

2. Resolution Analysis Using Diverse Test Images

The current study's focus on PSF metrics has yielded valuable insights into the sparse aperture system's performance. However, future work should aim to extend the analysis of the sparse aperture concept in terms of resolution, employing a broader range of test images that mimic real-world scenarios. This expansion will not only validate the system's capabilities in controlled environments but also its applicability in practical, operational settings.

The USAF resolution test chart can serve as an immediate next step. Analyzing the system's performance in resolving the fine details of the chart will provide a quantitative measure of the system's resolution capabilities. This will offer a more comprehensive understanding of the system's performance, complementing the PSF metrics. To further assess the system's operational efficacy, future studies should incorporate test images that represent potential surveillance targets. High-resolution images of ships, ground stations, and other structures of interest will gauge the system's readiness for real-world applications by analyzing its ability to resolve these images under various conditions and disturbances.

3. Sparse Aperture Testbed Improvements

The current sparse aperture testbed has provided valuable insights into the system's performance and its ability to correct aberrations. However, several enhancements are proposed to simulation formation aperture motion more accurately.

The current testbed setup limits the collector aperture piston motion peak to 20 µm, which may not fully represent the range of translational motion that satellite formations will encounter in space. Increasing this peak to 100 µm will allow for a more comprehensive simulation of the system's ability to correct for larger aberrations. This adjustment will provide a better understanding of the system's limits and its capability to maintain image quality under more extreme conditions.

The current testbed also utilizes a 0.25 m diameter collimator. Exploring the use of a 0.50 m diameter collimator could offer several advantages. A larger collimator would allow for the simulation of different fill fractions, which represent the ratio of the combined aperture area of the collector satellites to the total area encompassed by the formation. This would enable the study of sparse aperture systems with varying degrees of sparsity, providing insights into how fill fraction impacts image resolution and the effectiveness of correction algorithms.

4. Computer Modeling

Lastly, the MATLAB model of the L/F architecture simulates disturbances to provide an understanding of challenges the satellite formation might face. For enhanced fidelity in these simulations, future work should focus on incorporating a broader spectrum of frequencies and noise profiles that reflect the complex dynamics of space. This includes micro-vibrations from satellite subsystems, variations in orbital Incorporation of different thrusters, metrology systems, and other elements to simulate real conditions will be essential. This will help identify the most effective configurations and technologies for optimizing the satellite formation's operational performance. dynamics, and environmental perturbations impacting the stability of the formation.

Future efforts should also concentrate on translating these simulated disturbances into conditions applicable to the sparse aperture test table. This approach will subject the system’s correction algorithms to a more realistic testing environment, enabling refinement and ensuring robustness against real-world disturbances the satellite formation is likely to encounter.

THIS PAGE INTENTIONALLY LEFT BLANK

APPENDIX: MATLAB SCRIPT FOR TESTBED

```
%ZygoContecRealtime.m

if(exist('AO')) delete(AO);end; fclose all; clear all

%% INITIALIZE CONTEC BOARDS FOR COMPENSATOR PI CONTROLLERS

%open PI controllers for compensation stages, if not already open________
out = daqhwinfo           %informative only
out.InstalledAdaptors     %informative only
out = daqhwinfo('contec') %informative only for next line

AO=analogoutput('contec','AIO000')%the 1st installed card
addchannel(AO,0:8)%add 9 AO channels for use
AO.SampleRate=5000;%sounded good at the time
AO.TimerPeriod = 0.001;%not sure if it helps
AO.BufferingConfig=[1 2];%shrink default buffer for speed
%initialize positions to the midpoints on all channels to start
%Gain=10mRads/Volt Applied, limited to 0-3.5V, already biased by 1.75V in PI
%controllers
putdata(AO, [0.0 0.0    0.0 0.0    0.0 0.0    5.0 5.0 5.0]);start(AO);
disp('done initializing Contec AO channels');
disp('Compensators centered.');

disp('Adjust the Thorlabs controllers to center the three spots and optimize pistons.')
disp('Hit enter to use the compensators to hold these positions despite future Collector adjustments.')
pause;
disp('Thanks');

 %% INITIALIZE ETHERNET INTERFACE FOR ZYGO INTERFEROMETERS

%MIRROR positions viewed from front
%this is the order that they appear in the VME Chassis Rack from top to bot

%WAVELENGTH COMPENSATOR
t6 = tcpip('169.254.74.66',1500);t6.timeout = .00001;fopen(t6); %A1=F10 WavelengthComp
fprintf(t6,':ZMI:REG:WRIT:AXIS1:WORD #H0,#H1');

%BOTTOM RIGHT MIRROR
fprintf(t6,':ZMI:REG:WRIT:AXIS2:WORD #H0,#H1');                 %A2=F1 MBR BRC
t2 = tcpip('169.254.74.62',1500);t2.timeout = .00001;fopen(t2); %A1=F2 MBR BL
fprintf(t2,':ZMI:REG:WRIT:AXIS1:WORD #H0,#H1');                 %A2=F3 MBR TR
%BOTTOM LEFT MIRROR positions viewed from front
```

```
fprintf(t2,':ZMI:REG:WRIT:AXIS2:WORD #H0,#H1');
t3 = tcpip('169.254.74.63',1500);t3.timeout = .00001;fopen(t3); %A1=F4 MBL BLC
fprintf(t3,':ZMI:REG:WRIT:AXIS1:WORD #H0,#H1');                 %A2=F5 MBL BR
fprintf(t3,':ZMI:REG:WRIT:AXIS2:WORD #H0,#H1');
t4 = tcpip('169.254.74.64',1500);t4.timeout = .00001;fopen(t4); %A1=F6 MBL TL

%TOP CENTER MIRROR positions viewed from front
fprintf(t4,':ZMI:REG:WRIT:AXIS1:WORD #H0,#H1');                 %A2=F7 MTC TLC
fprintf(t4,':ZMI:REG:WRIT:AXIS2:WORD #H0,#H1');
t5 = tcpip('169.254.74.65',1500);t5.timeout = .00001;fopen(t5); %A1=F8 MTC TR
fprintf(t5,':ZMI:REG:WRIT:AXIS1:WORD #H0,#H1');                 %A2=F9 MTC BL
fprintf(t5,':ZMI:REG:WRIT:AXIS2:WORD #H0,#H1');

%res=fread(t1);%throw away
res=fread(t2);%throw away
res=fread(t3);%throw away
res=fread(t4);%throw away
res=fread(t5);%throw away
res=fread(t6);%throw away

%res=fread(t1);%throw away more
res=fread(t2);%throw away
res=fread(t3);%throw away
res=fread(t4);%throw away
res=fread(t5);%throw away
res=fread(t6);%throw away

%% BEGIN CORRECTION LOOP
disp('beginning correction loop');

 %% Do 25 rounds of corrections
 for i1=1:25

%% ACQUIRE DATA FROM EACH INTERFEROMETER
fprintf(t6,':MEAS:AXIS2:FULL:POS?'); %request a measurement be made     t6 AXIS2
res=char(fread(t6,11));%read the measurement into matlab              t6
%conversion to a decimal number
n=res(3:11)';%these are the characters we care about that make the number in hex array
n=hex2dec(n);%each hex number is now a decimal number in each array position
s=n;
% %correct for wrap-around around 0 and FFFFFFFFF
 midpoint=(2^36)/2-1;max=2^36; if s>midpoint s=s-max;end; meas(1) = int64(s);

 fprintf(t2,':MEAS:AXIS1:FULL:POS?'); %request a measurement be made
res=char(fread(t2,11));%read the measurement into matlab
%conversion to a decimal number
n=res(3:11)';%these are the characters we care about that make the number in hex array
```

```matlab
n=hex2dec(n);%each hex number is now a decimal number in each array position
s=n;
% %correct for wrap-around around 0 and FFFFFFFFF
 midpoint=(2^36)/2-1;max=2^36; if s>midpoint s=s-max;end; meas(2) = int64(s);

fprintf(t2,':MEAS:AXIS2:FULL:POS?'); %request a measurement be made
res=char(fread(t2,11));%read the measurement into matlab
%conversion to a decimal number
n=res(3:11)';%these are the characters we care about that make the number in hex array
n=hex2dec(n);%each hex number is now a decimal number in each array position
s=n;
% %correct for wrap-around around 0 and FFFFFFFFF
 midpoint=(2^36)/2-1;max=2^36; if s>midpoint s=s-max;end; meas(3) = int64(s);

fprintf(t3,':MEAS:AXIS1:FULL:POS?'); %request a measurement be made
res=char(fread(t3,11));%read the measurement into matlab
%conversion to a decimal number
n=res(3:11)';%these are the characters we care about that make the number in hex array
n=hex2dec(n);%each hex number is now a decimal number in each array position
s=n;
% %correct for wrap-around around 0 and FFFFFFFFF
 midpoint=(2^36)/2-1;max=2^36; if s>midpoint s=s-max;end; meas(4) = int64(s);

fprintf(t3,':MEAS:AXIS2:FULL:POS?'); %request a measurement be made
res=char(fread(t3,11));%read the measurement into matlab
%conversion to a decimal number
n=res(3:11)';%these are the characters we care about that make the number in hex array
n=hex2dec(n);%each hex number is now a decimal number in each array position
s=n;
% %correct for wrap-around around 0 and FFFFFFFFF
 midpoint=(2^36)/2-1;max=2^36; if s>midpoint s=s-max;end; meas(5) = int64(s);

fprintf(t4,':MEAS:AXIS1:FULL:POS?'); %request a measurement be made
res=char(fread(t4,11));%read the measurement into matlab
%conversion to a decimal number
n=res(3:11)';%these are the characters we care about that make the number in hex array
n=hex2dec(n);%each hex number is now a decimal number in each array position
s=n;
% %correct for wrap-around around 0 and FFFFFFFFF
 midpoint=(2^36)/2-1;max=2^36; if s>midpoint s=s-max;end;meas(6) = int64(s);

fprintf(t4,':MEAS:AXIS2:FULL:POS?'); %request a measurement be made
res=char(fread(t4,11));%read the measurement into matlab
%conversion to a decimal number
n=res(3:11)';%these are the characters we care about that make the number in hex array
n=hex2dec(n);%each hex number is now a decimal number in each array position
s=n;
```

```
% %correct for wrap-around around 0 and FFFFFFFFF
 midpoint=(2^36)/2-1;max=2^36; if s>midpoint s=s-max;end;meas(7) = int64(s);

fprintf(t5,':MEAS:AXIS1:FULL:POS?'); %request a measurement be made
res=char(fread(t5,11));%read the measurement into matlab
%conversion to a decimal number
n=res(3:11)';%these are the characters we care about that make the number in hex array
n=hex2dec(n);%each hex number is now a decimal number in each array position
s=n;
% %correct for wrap-around around 0 and FFFFFFFFF
 midpoint=(2^36)/2-1;max=2^36; if s>midpoint s=s-max;end; meas(8) = int64(s);

fprintf(t5,':MEAS:AXIS2:FULL:POS?'); %request a measurement be made
res=char(fread(t5,11));%read the measurement into matlab
%conversion to a decimal number
n=res(3:11)';%these are the characters we care about that make the number in hex array
n=hex2dec(n);%each hex number is now a decimal number in each array position
s=n;
% %correct for wrap-around around 0 and FFFFFFFFF
 midpoint=(2^36)/2-1;max=2^36; if s>midpoint s=s-max;end; meas(9) = int64(s);

fprintf(t6,':MEAS:AXIS1:FULL:POS?'); %request a measurement be made
res=char(fread(t6,11));%read the measurement into matlab
%conversion to a decimal number
n=res(3:11)';%these are the characters we care about that make the number in hex array
n=hex2dec(n);%each hex number is now a decimal number in each array position
s=n;
% %correct for wrap-around around 0 and FFFFFFFFF
 midpoint=(2^36)/2-1;max=2^36; if s>midpoint s=s-max;end; meas(10) = int64(s);
    %% Convert to meters
    meas=double(meas);m=meas(1:9);
    LambdaV=632.991501e-9;%F1 vertical pol (larger distance increases counts)
    LambdaH=632.991528e-9;%F2 horiz pol (larger distance decreases counts)
    m=m*LambdaH/1024;

    %% Apply Wavelength compensation
        D=3.0;%meters of deadpath
        n0=1.00027;%refractive index at STP conditions
        Ncwc=meas(10);%number of counts
        Lambdacwc_v=LambdaV;%vertical pol wavelength of laser
        M=512;%for ZMI2402 readout
        Lcell=70.03e-3;%vacuum cell length
        deltaN=Ncwc*Lambdacwc_v/(4*M*Lcell);
        n=n0-deltaN;
        m=m-D*(1-n/n0);%probably the correct sign, but also likely insignificant
        wavelength_compensation = [wavelength_compensation; deltaN];
```

```
%% Raw Tilts and Pistons Calculations (in Radians and meters)
%Bottom Right Mirror (viewed from front)
   Tbrx=(m(1)-m(2))/.0421; Tbry=(m(1)-m(3))/.0421; Pbr=m(1)-m(2)-m(3);
%Bottom Left Mirror
   Tblx=(m(5)-m(4))/.0421; Tbly=(m(4)-m(6))/.0421; Pbl=m(4)-m(5)-m(6);
%Top Center Mirror
   Ttcx=(m(8)-m(7))/.0421; Ttcy=(m(9)-m(7))/.0421; Ptc=m(7)-m(8)-m(9);
%% Plot Metrology Data in 3D Bar Plot
ms=zeros(1,11);
ms(1:3)=m(4:6);
ms(5:7)=m(7:9);
ms(9:11)=m(1:3);
bar(ms);axis([0 12 -10e-6 10e-6]);grid on;
title('Zygo Metrology System Measurements')
xlabel('9ea. actuators in groups of 3, (Corner, X, Y)');
ylabel('displacements[meters]');
text(1,-1.2e-5,'Bottom Left');text(5,-1.2e-5,'Top Center');text(9,-1.2e-5,'Bottom Right');
drawnow;

%% convert angles from Rads to mRads
Tbrx=Tbrx*1000;    Tbry=Tbry*1000;%mRads
Tblx=Tblx*1000;    Tbly=Tbly*1000;%mRads
Ttcx=Ttcx*1000;    Ttcy=Ttcy*1000;%mRads

%% Saturate Zygo Tip/Tilt values -17.5 to 17.5 mRads, offset by +17.5mRads
if(Tbrx<-17.5);Tbrx=-17.5;end;  if(Tbrx>17.5);Tbrx=17.5;end;
if(Tbry<-17.5);Tbry=-17.5;end;  if(Tbry>17.5);Tbry=17.5;end;
if(Tblx<-17.5);Tblx=-17.5;end;  if(Tblx>17.5);Tblx=17.5;end;
if(Tbly<-17.5);Tbly=-17.5;end;  if(Tbly>17.5);Tbly=17.5;end;
if(Ttcx<-17.5);Ttcx=-17.5;end;  if(Ttcx>17.5);Ttcx=17.5;end;
if(Ttcy<-17.5);Ttcy=-17.5;end;  if(Ttcy>17.5);Ttcy=17.5;end;

%2x angle increase is caused by 2x beam reduction in optical system
%but the drive angle for tip/tilt is defined as mechanical, not optical,
%so the optical angle is already 2x, so no adjustment is needed
%And Piston is Piston, but the sign for the compensator is decreasing
%optical path for increasing value in microns

%% convert Pistons from meters to microns needed by controllers
Pbr=Pbr*1e6;    Pbl=Pbl*1e6;    Ptc=Ptc*1e6;%microns
%saturate Piston values to be within -50 to +50 um and offset by +50um
if(Pbr<-50.0);Pbr=-50.0;end;  if(Pbr>50.0);Pbr=50.0;end;
if(Pbl<-50.0);Pbl=-50.0;end;  if(Pbl>50.0);Pbl=50.0;end;
if(Ptc<-50.0);Ptc=-50.0;end;  if(Ptc>50.0);Ptc=50.0;end;
figure; % Create a new figure

%% Calculate corrections to compensating mirrors and scale voltage down
```

```
    x=Tblx*1.14-Tbly*0.015;   y=Tbly*1.07-Tblx*0.055;%done
    Mbl1=(sqrt(2)*( x-y))*10;%offset removed, put into controller
    Mbl2=(sqrt(2)*(-x-y))*10;%and mult gain by 100X

    x=Ttcx*1.14+Ttcy*0.025;   y=Ttcy*1.19-Ttcx*0.01;%done
    Mtc1=(sqrt(2)*( x-y))*10.0;%offset removed, put into controller
    Mtc2=(sqrt(2)*(-x-y))*10.0;%and mult gain by 100X

    x=Tbrx*1.14-Tbry*.09;    y=Tbry*1.05+.055*Tbrx;%done
    Mbr1=(sqrt(2)*(-x+y))*10;%offset removed, put into controller
    Mbr2=(sqrt(2)*(+x+y))*10;%and mult gain by 100X

    Pbr=(-Pbr+50.0)/10;Zbr=Pbr;
    Pbl=(-Pbl+50.0)/10;Zbl=Pbl;
    Ptc=(-Ptc+50.0)/10;Ztc=Ptc;

    putdata(AO, [Mbr1 Mbr2 Mbl1 Mbl2 Mtc1 Mtc2 Ztc Zbl Zbr]);start(AO);

 end
end
%% DE-INITIALIZE EVERYTHING

%delete(AO1);
%fclose(t1);delete(t1) %no longer used
fclose(t2);delete(t2)
fclose(t3);delete(t3)
fclose(t4);delete(t4)
fclose(t5);delete(t5)
fclose(t6);delete(t6)
% fclose(t7);delete(t7)
% fclose(t8);delete(t8)
% fclose(t9);delete(t9)
% fclose(t10);delete(t10)
delete(AO);fclose all; clear all
```

LIST OF REFERENCES

[1] S.-J. Chung, "Design, implementation and control of a sparse aperture imaging satellite," M.S. thesis, Dept. of Aeronautics and Astronautics, MIT, Cambridge, MA, USA, 2002. Available: https://dspace.mit.edu/handle/1721.1/39262

[2] A. B. Meinel, "Cost-scaling laws applicable to very large optical telescopes," *Opt. Eng.*, vol. 18, no. 6, pp. 645–647, Dec. 1979. Available: https://doi.org/10.1117/12.7972448

[3] "James Webb space telescope," *Wikipedia*. Accessed: Oct. 23, 2023. Available: https://en.wikipedia.org/w/index.php?title=James_Webb_Space_Telescope&oldid=1181458114

[4] S. Sundey, "Design and implementation of an optical sparse aperture testbed for small satellite formation space-based remote sensing," M.S. thesis, Dept. of Space Systems Eng., NPS, Monterey, CA, USA, 2009.

[5] N. J. Miller, M. P. Dierking, and B. D. Duncan, "Optical sparse aperture imaging," *Appl. Opt.*, vol. 46, no. 23, pp. 5933–5943, Aug. 2007. Available: doi: 10.1364/AO.46.005933

[6] National Aviation and Space Agency, "What are SmallSats and CubeSats?." Accessed: Oct. 25, 2023. Available: https://www.nasa.gov/what-are-smallsats-and-cubesats/

[7] S. W. Paek, S. Balasubramanian, S. Kim, and O. de Weck, "Small-satellite synthetic aperture radar for continuous global biospheric monitoring: A review," *Remote Sensing*, vol. 12, no. 16, pp. 2546–2577, Aug. 2020. Available: doi: 10.3390/rs12162546

[8] "Small satellite," *Wikipedia*. Accessed: Sep. 18, 2023. Available: https://en.wikipedia.org/w/index.php?title=Small_satellite&oldid=1164723323

[9] K. M. Wagner and J. T. Black, "Design of a resilient rideshare-based small satellite constellation using a genetic algorithm," presented at *AAS/AIAA Space Flight Mechanics Meeting*, Portland, ME, USA, Aug 11–15, 2019. Available: https://vsgc.odu.edu/wp-content/uploads/2019/05/Katherine-Mott.pdf

[10] C. Seubert, D. Sharf, D. Morgan, H. Chang, P. Bruigarolas, F. Hadaegh, D. Redding, J. Lou, and C. Frazen, "Distributed aperture formation control in MEO," presented at the *National Aeronautics and Space Administration Jet Propulsion Laboratory California Institute of Technology*, Pasadena, CA, USA, Nov. 22, 2013.

[11] S.-J. Chung, D. W. Miller, and O. L. De Weck, "Design and implementation of sparse aperture imaging systems," *Highly Innovative Space Telescope Concepts*, vol. 4849, pp. 181–192, Dec. 2002. Available: doi: 10.1117/12.460077

[12] National Institute of Standards and Technology, "Metrology," Jun. 2016, Available: https://www.nist.gov/metrology

[13] J. Qian, X. Wu, H. Liu, X. Hua, Y. Tao, and R. Zhang, "The structure research and design for beam steering and adjustment in Golay3 sparse-aperture imaging system," *Appl. Sci.*, vol. 12, no. 8, pp. 1–14, Apr. 2022. Available: doi: 10.3390/app12084003

[14] B. Agrawal and J. J. Kim, "Naval Postgraduate School (NPS) proposal for research: Research on sparse aperture systems," unpublished.

[15] Newport, "RS4000 optical table top." Accessed: Oct. 27, 2023. Available: https://www.newport.com/f/tuned-damped-top-performance-optical-tables

[16] Thorlabs, "6-Axis NanoMax^{TM} nanopositioning flexure stages." Accessed: Oct. 27, 2023. Available: https://www.thorlabs.com/newgrouppage9.cfm?objectgroup_id=1100

[17] J. Baker, "2017 Final report sparse aperture array (rev.1)," unpublished.

[18] Thorlabs, "150 V USB closed-loop piezo controllers." Accessed: Oct. 27, 2023. Available: https://www.thorlabs.com/newgrouppage9.cfm?objectgroup_id=1912

[19] Lambda, *ZMI 7702 laser head.* 2020. Available: https://www.lambdaphoto.co.uk/pdfs/Zygo/LAMBDA_zmi-7702-laser-head-specs.pdf

[20] GlobalSpec, "Corner cube retroreflectors from Zygo corporation." Accessed: Oct. 30, 2023. Available: https://www.globalspec.com/FeaturedProducts/Detail/ZygoCorporation/Corner_Cube_Retroreflectors/295493/0?fromSpotlight=1

[21] LAMBDA, *ZMI 2400 Measurement Board.* 2018. Available: https://www.lambdaphoto.co.uk/pdfs/Zygo/LAMBDA_zmi-2400-measurement-board-specs.pdf

[22] Physik Instrumente, *Piezo Tip/Tilt platform*. 2020. Available: https://www.pi-usa.us/fileadmin/user_upload/physik_instrumente/files/datasheets/S-335-Datasheet.pdf

[23] Physik Instrumente, *PIHera piezo linear precision positioner.* 2022. Available: https://www.pi-usa.us/en/products/piezo-flexure-nanopositioners/x-linear-piezo-flexure-nanopositioning-stages/p-6201-p-6291-pihera-piezo-linear-stage-202300

[24] Imaging Development Systems, *UI-1540LE-M-GL rev.2 (ABO2536)*. 2023. Available: https://www.ids-imaging.us/download-details/AB02536.html

[25] MathWorks, "Modeling custom satellite attitude and gimbal steering – MATLAB & Simulink." Accessed: Nov. 01, 2023. Available: https://www.mathworks.com/help/satcom/ug/modeling-custom-satellite-attitude-and-gimbal-steering.html

[26] Space Telescope Science Institute, "6.5 Signal-to-Noise ratio estimation." Accessed: Oct. 30, 2023. Available: https://www.stsci.edu/instruments/wfpc2/Wfpc2_hand6/ch6_exposuretime6.html

[27] "Root-mean-square deviation," *Wikipedia*. Accessed: Oct. 08, 2023. Available: https://en.wikipedia.org/w/index.php?title=Root-mean-square_deviation&oldid=1179174918

THIS PAGE INTENTIONALLY LEFT BLANK

INITIAL DISTRIBUTION LIST

1. Defense Technical Information Center
   Fort Belvoir, Virginia

2. Dudley Knox Library
   Naval Postgraduate School
   Monterey, California